

Organization of Tropical Convection in Low Vertical Wind Shears: The Role of Cold Pools

ADRIAN M. TOMPKINS*

Max-Planck-Institut für Meteorologie, Hamburg, Germany

(Manuscript received 18 January 2000, in final form 20 October 2000)

ABSTRACT

An investigation is conducted to document the role convectively generated cold pools play in determining the spatial organization of tropical deep convection. Using a high-resolution cloud-resolving model, the evolution of cold pools produced by deep convection is examined, in the situation of limited large-scale wind shear, and a homogeneous underlying sea surface temperature. Ignoring the cold pools resulting from multiple deep convective events, the mean model cold pool attained a minimum temperature and water vapor mixing ratio depression of 1 K and 1.5 g kg^{-1} , respectively; a horizontal velocity increase of 4.8 m s^{-1} ; and the latent and sensible heat fluxes are increased by a factor of 1.9 and 2.6, respectively. The cold pools had a mean lifetime of approximately 2.5 h and attained maximum radii ranging from 3 to 18 km, with a mean of 8.6 km. Taking the organization of convection into account, these figures are consistent with observational studies of convective wakes.

The composite cold pool showed that development occurred in three distinct stages. As seen in observations, the air in the vicinity of deep convection has a higher equivalent potential energy than average. In the first stage, before the downdraft develops and reaches the subcloud layer, the area below the convection is cooled and moistened by the evaporation of rainfall. The downdraft then injects cold and dry air into the boundary layer, and the spreading cold pool is consequentially moister than average just inside the gust front but drier in the central regions. Finally, mass conservation requires that air from above the boundary layer be entrained into the wake of the expiring downdraft—thus causing the central regions of the cold pool to recover very quickly in temperature—but increases further the moisture perturbation. These features are confirmed by a number of observational studies.

The key to the triggering of new deep convective cells lies with the band of high equivalent potential temperature, but negatively buoyant air, situated inside the boundary of the spreading cold pools. It is this air that forms the new convective cells. The radius at which this occurs is determined by the time taken for surface fluxes to remove the negative temperature perturbation, thereby reducing convective inhibition energy. In summary, the primary mechanism by which cold pools organize tropical deep convection in low wind shear conditions is principally thermodynamical, and not dynamical as previously assumed.

1. Introduction

Observations in the Tropics have shown that convection can exist as isolated thunderstorms distributed in an apparently random or clustered fashion, or can be linearly or nonlinearly organized into larger systems such as squall lines or mesoscale convective systems (MCSs) (e.g., Houze and Betts 1981; Mapes and Houze 1992; Rickenbach and Rutledge 1998). Since the temporal and spatial organization of convection has a dramatic effect on the convective transports of heat, moisture, and momentum, it is crucial to understand the factors that determine this. Recognition of this has led to

the first attempts to start including the organization of convection into parameterization schemes in general circulation models (Moncrieff and Klinker 1997).

The general spatial distribution of convection can be associated with sea surface temperature (SST) gradients (Graham and Barnett 1987; Lau et al. 1997; Bony et al. 1997), and it is well known that factors such as vertical wind shear can act to organize convection into larger mesoscale systems (e.g., Rotunno et al. 1988; LeMone et al. 1998), and that the intrusion of dry air can strongly modulate convective activity (e.g., Yoneyama and Fujitani 1995; Mapes and Zuidema 1996; Brown and Zhang 1997; Yoneyama and Parsons 1999). In addition to these well-known organizing mechanisms, there are other feedback processes that could organize convection and that are less well understood. For example, localized convective moistening of the atmosphere (Nicholls and LeMone 1980; Randall and Huffman 1980), or convective initiation due to convectively generated cold pools

* Current affiliation: ECMWF, Reading, United Kingdom.

Corresponding author address: Dr. Adrian M. Tompkins, ECMWF, Shinfield Park, Reading RG2 9AX, United Kingdom.
E-mail: tompkins@ecmwf.int

(Thorpe et al. 1982), or gravity waves (Mapes 1993) could each be involved in the organization of convection on a variety of spatial scales. Observations appear to show that clouds associated with shallow convection can be clustered, randomly or regularly distributed, depending on the spatial scale analyzed (e.g., Sengupta et al. 1990; Zhu et al. 1992; Weger et al. 1993; Nair et al. 1998), but it is difficult to ascertain from observations what the causes are for any organization existing, and on what temporal and spatial scales they operate.

Cloud-resolving models (CRMs), explicitly representing cloud-scale dynamics, offer a useful tool to investigate the spontaneous organization of convection since controlled experiments can be conducted in which external organizing factors such as wind shear and large-scale flow can be prescribed. Unfortunately, in the past, computing resources have restricted CRM experiments to either small three-dimensional domains that were too limited in extent to reveal any mesoscale organization of convection, or to two-dimensional simulations that place artificial constraints on the generated circulations (Tompkins 2000).

Recently, however, some attempts at larger-domain long-term cloud simulation have been accomplished. For example, Grabowski et al. (1998) made weeklong 3D simulations of convection in the Global Atmospheric Research Programme (GARP) Atlantic Tropical Experiment (GATE), where organization was strongly constrained by the imposed large-scale forcing. Tompkins and Craig (1998) conducted long-term simulations without large-scale forcing, and found that the interaction between radiation and convection acted strongly to organize the convection into bands. However, the domain used was quite restricted at only 100 by 100 km². Tompkins (2001) operated a 3D CRM over a time period of 20 days, using a compromise domain configuration that was over 1000 km in one lateral direction to allow mesoscale organization to occur, but having a third spatial dimension of 64 km so that the circulation was not artificially constrained. They found that spontaneous organization of convection did indeed occur after 4 or 5 days of simulation, taking the form of distinct cloud clusters of approximately 200 km in dimension, separated by clear-sky regions of order 100 km in scale free of deep and often shallow convection. The clusters propagated slowly through the domain, while small convective systems propagated through the clusters themselves. The mesoscale clustering of convection was shown to be the result of a positive feedback between the water vapor field and deep convective activity.

Additionally, Tompkins (2001) observed that, within the convective clusters themselves, new convective events often seemed to be initiated on the boundaries of cold pool outflow from previous cumulus towers. Downdrafts have long been recognized as an important component of convective systems in terms of their thermodynamic effects (e.g., Zipser 1977), and Simpson (1980) suggested that they could play a role in the ini-

tiation of new convective events. This role was subsequently observed in both modeling studies and observations (e.g., Wilhelmson and Chen 1982; Peterson 1984). Despite the fact that this triggering role was recognized as central in the propagation of squall lines (Moncrieff 1981; Thorpe et al. 1982), the importance of convective cold pool triggering of new convective cells has been relatively ignored until recent attempts to include it in a simple tropical model (Mapes 2000). The triggering role of cold pools has been largely attributed to their dynamical action of lifting the environmental boundary layer at the cold pool front through its negatively buoyant convective inhibition (CIN) layer, allowing free convection to commence (Emanuel 1994). Indeed, this role has been observed in a number of numerical studies of cold pool outflow (e.g., Xue et al. 1997; Fovell and Tan 1998; Lin et al. 1998).

In the simulations of Tompkins (2001) it was noted that the cold pools did not trigger convection soon after their formation, when the outflow velocities and cold pool depth (and therefore the dynamical lifting) would be at a maximum. Rather, the cold pools would spread out to radii of up to 30 km, although more typically 8 to 15 km, over a period of a few hours, before new convection was triggered at their boundaries. At this distance, the signature of the cold pool in terms of the vertically lifted air at the gust front boundary was almost imperceptible. In fact, "gust front" is no longer a suitable term for the cold pool boundary since propagation velocities were also practically zero by this point. Instead, the cold pool signature consisted of a small temperature depression that was still apparent, and also by the fingerprint in the water vapor field. This was, in fact, the most remarkable feature, since, although the inner region of the cold pool was dryer than the boundary layer mean as expected, the outer regions of the cold pool were actually found to be moister than average. This meant that, in despite of the small temperature depression that continued to exist at the convective wake boundary, the equivalent potential temperature (θ_e), and thus the associated value of convective available potential energy (CAPE), was greater inside the cold pool boundaries than anywhere else in the model domain. This raised the possibility that while squall lines propagate through the dynamical action of convective wakes, the equally prevalent scattered "popcorn" deep convection in the Tropics could propagate through their thermodynamical role.

The aim of this paper is to investigate this hypothesis further. For example, the origin of the high water vapor amounts on the edges of the downdrafts is not clear. Downdrafts are known to significantly enhance surface fluxes (Johnson and Nicholls 1983; Addis et al. 1984; Young et al. 1995; Jabouille et al. 1996) due to the dry, cold perturbation within the downdrafts, and also because of the enhanced wind speeds. Therefore it is possible that wind-enhanced fluxes cause the wake water vapor to recover more quickly than temperature, pro-

ducing positive perturbations and associated high CAPE within the gust front of older established wakes. While this was exactly the behavior produced in the wake model of Qian et al. (1998), observations often show limited water vapor recovery (Houze and Betts 1981; Young et al. 1995).

The approach is to use a CRM to study cold pool development, with particular regard paid to interaction with the water vapor field evolution. There have been numerous previous numerical investigations of cold pools, which have revealed much about the way cold pools propagate and evolve in various environment conditions such as stratification or wind shear (e.g., Droege-meier and Wilhelmson 1987; Liu and Moncrieff 1996; Xu et al. 1996; Xue et al. 1997; Moncrieff and Liu 1999; Liu and Moncrieff 2000). However, in order to be able to carefully control the environmental conditions, these previous investigations often used the approach of studying single density current cases, which were artificially initialized, for example by imposing a time-invariant cold source. It is not clear how well the thermodynamic structure of the resulting cold pools resembles those of real systems, particularly with regard to the role of the water vapor field. Therefore we adopt the approach of simulating a field of deep convective clouds in a state of radiative–convective equilibrium and then conditionally sample the resulting cold pools to gain composite statistics such as those derived from observational studies. Using this approach the thermodynamical structure of the cold pools will be as realistic as possible, bearing in mind the limitation of our knowledge concerning certain processes represented in the model, such as cloud microphysics for example.

Section 2 outlines the numerical simulations conducted and section 3 then examines the evolution of individual examples of cold pools in some detail. The following section examines the cold pool composite statistics to gain a more generalized understanding of the cold pool evolution. Finally, a comparison with previous observational studies is carried out and it is shown that they can be better understood in light of the results of the numerical experiments conducted.

2. Numerical model

a. Model description and experimental setup

A detailed description of the CRM used for the numerical experiments is contained in Tompkins and Craig (1998) and references therein, with modifications described in Tompkins (2001). The basic cloud model is anelastic with an advanced total variation diminishing scheme for advection of all prognostic quantities (Leonard 1991). The microphysical scheme integrates prognostic equations for rain, snow, cloud water, cloud ice, and graupel amounts, and also the ice crystal concentration number (Brown and Swann 1997). The surface fluxes are provided using similarity theory based on Eqs.

(3.23), (3.24), (3.29), and (3.33) of Garratt (1992), with constants given in Tompkins and Craig (1998). Implicit in this approach is the assumption that similarity functions for temperature and water vapor are identical, and that the bottom model level at 50 m is situated within the surface layer. The advantage of this implementation is that it renders realistic fluxes in zero wind conditions and therefore obviates the requirement to impose an artificial minimum surface wind speed often necessary if a bulk aerodynamic formula is used. The formulation produces a similar wind sensitivity of surface fluxes to observations by Jabouille et al. (1996). The surface was assumed to be ocean with a fixed horizontally homogeneous temperature of 300 K.

Regarding the setup of the model domain, Tompkins (2000) demonstrated that two-dimensional simulations artificially impose a large-scale organization on convection and therefore a 3D domain was used. Since the horizontal scales of the spreading cold pools are on the order of 10 km it is likely that they are poorly resolved by the 2-km resolution used in Tompkins (2001). As the focus of this study is on the cold pools themselves, and not the large-scale organization they lead to, a smaller domain was chosen of 89.6 km on each side, but with a high horizontal resolution of 350 m in an attempt to better resolve the cold pools. The extent of the domain size is still adequate to contain many concurrent deep convection events with the radiative forcing rate used of 2 K day^{-1} .

The experiment lasted for a period of 24 h. However, for this relatively short integration length, it is essential that the initial conditions are not an artificial resting state, but already contain a field of realistic deep convective clouds, preferably with the model fields near their “natural” radiative convection equilibrium state. Therefore, the model was operated at a lower horizontal resolution of 1.4 km for a period of 10 days. This is sufficient to allow the model to settle into a quasi-steady state in which the long-term tendencies of the model fields are limited. At this point the model fields were converted to the high-resolution grid of 350 m, and the model was integrated for a further 6 h to allow any minor spurious wave activity caused by the grid conversion process to dissipate. The model state at the end of this period was used as the initial conditions for the 24-h experiment from which statistics are shown in this paper. Note that the full equilibrium state for the model using 350 m is unlikely to be same as that for the coarser 2-km resolution (i.e., the model has probably not converged with increasing resolution at 2 km, or indeed even at 350 m). However, it is presumed that the differences in background mean model states will not drastically alter the first-order behavior and characteristics of the convection and cold pools simulated. All other setup details, such as the forcing profile and vertical grid, were identical to Tompkins (2001).

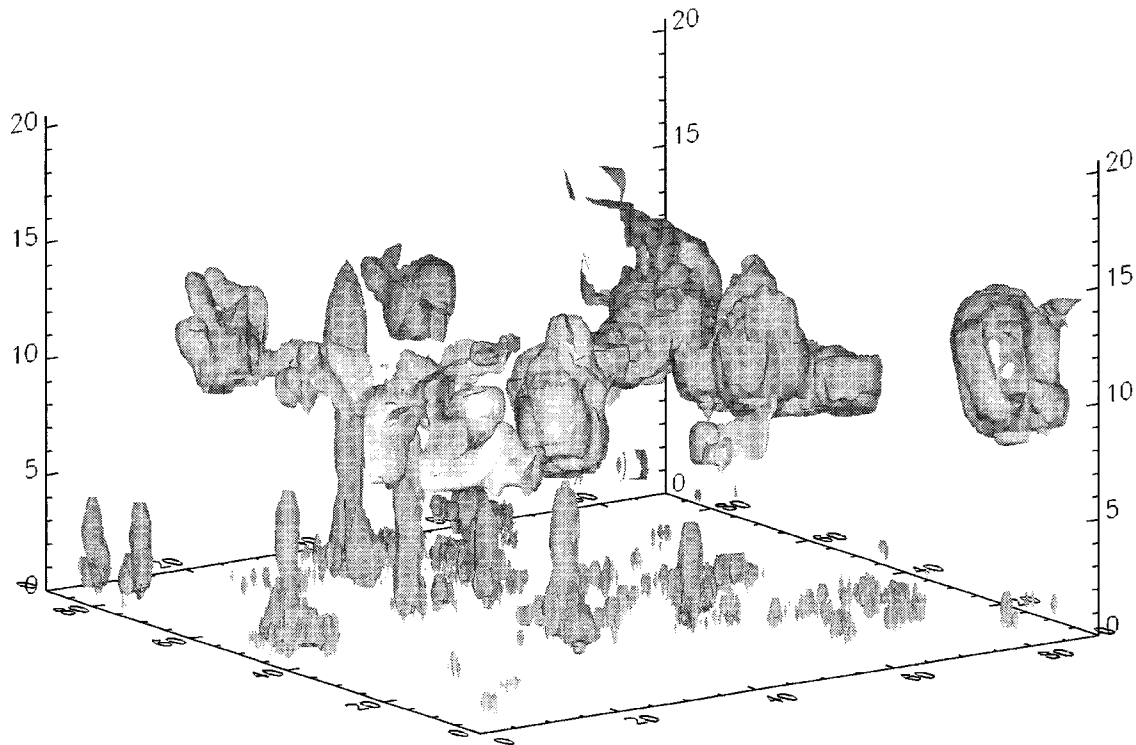


FIG. 1. Snapshot of total cloud condensate (ice + liquid) taken 30 min into the simulation. The surface indicates a cloud mass mixing ratio of $5 \times 10^{-6} \text{ kg kg}^{-1}$.

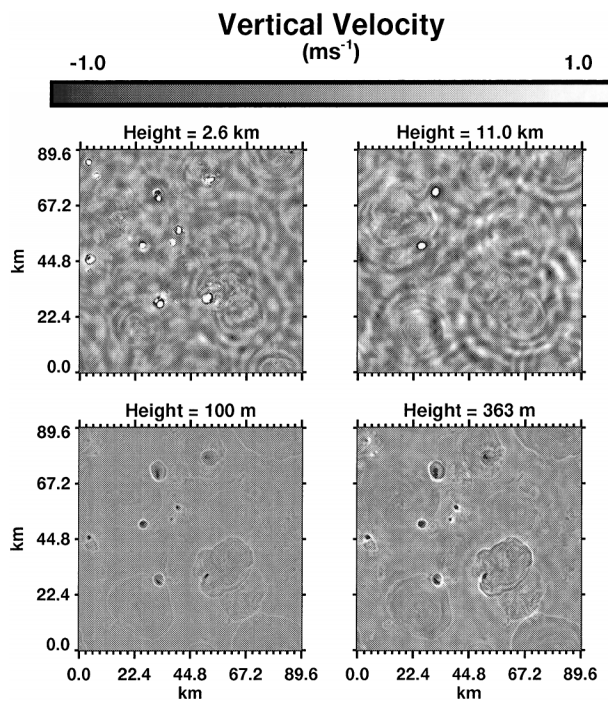


FIG. 2. Slices of the vertical velocity taken at heights of 100 m, 363 m, 2.6 km, and 11 km. In order to show the fine detail the color scale is cut off at a maximum and minimum velocity of 1 and -1 m s^{-1} , respectively, but velocities far in excess of this exist in the convective cores.

b. Convection in initial state

In order to show the realism of the simulated clouds and the nature of the organization that exists in these experiments, this section introduces various model fields taken 30 min into the simulation. This time period was chosen simply because of a greater abundance of newly formed cold pools present, but otherwise the model state remains quantitatively similar throughout the simulation period.

The three-dimensional cloud field boundary (Fig. 1) reveals an abundance of cloud present in the domain. The tall cylinder-like cloud forms on the left side of the figure represent the cloud in convectively active vertical updraft cores. Although the exact number of cores is not clear from this picture, it is obvious that the domain is large enough to contain many active convective events of various sizes concurrently. Also clear are the many detached anvil clouds that remain from previous convective events. On the right-hand side of the diagram, many examples of shallow cloud are visible, which are mostly examples of arcus-type cloud resulting from the forced ascent at the edges of spreading cold pools.

To gain a clearer picture of how the convection is actually organized within the domain, Fig. 2 shows the vertical velocity taken at four horizontal slices within the domain. Focusing first on the bottom left panel taken at a height of 100 m (the lowest model level for velocity

since the model uses an Arakawa C grid) it is possible to identify the cold pool areas by the ring of uplifted air at the convergence zone on their outer edges. The upward velocities are quite large on the edges of the smaller new cold pool, reaching as much as 0.8 m s^{-1} . This is almost twice as large as those commonly seen in the simulations of Tompkins (2001), probably due to the finer horizontal resolution used here (350 m compared to 2 km). Another consequence of the higher resolution is that the cold pools are visible in the velocity field at much larger radii. In coarse-resolution simulations the uplifting of air was not discernible once the cold pool attained a radius exceeding approximately 15 km, but with the higher horizontal resolution it is possible to resolve a very fine band of uplifted air even at these radii. The vertical velocities, however, are very weak once the cold pool reaches this size, usually not exceeding 0.05 m s^{-1} in magnitude. The panel for the height of 363 m, higher in the boundary layer (bottom right), shows similar features to the 100-m level, but the vertical velocities are seen to be larger at this height, and the width of the convergence zones is also marginally greater.

Examining vertical velocity at 2.6 km (Fig. 2, upper left), above the height at which the many shallow convective clouds terminate, reveals the presence of many convective cores that reach at least midlevels. The velocity is shown with a scale ranging from -1 to $+1 \text{ m s}^{-1}$ in order to reveal the distinct circular patterns of gravity waves propagating outward from the convective sources. Therefore, the convective cores, with velocities exceeding 1 m s^{-1} , a commonly used criterion for identifying convective up- and downdrafts (e.g., LeMone and Zipser 1980; Jorgensen and LeMone 1989; Lucas et al. 1994), appear as bright white patches. Vertical velocities within deep convective cores generally obtain maximum magnitudes between 10 and 20 m s^{-1} in the upper troposphere. At 2.6 km at this particular instant in time, 10 convective cores of substantial size are visible. At the horizontal resolution used, the cores are reasonably well resolved, consisting of at least 20 grid points. The convection appears to be quite clustered, with the majority of convection occurring in the upper left quadrant of the domain. Examining the cores closely, the structure is visible as a fairly circular updraft core surrounded by a ring of downdraft air. However, the structure is sometimes more complex. For example, in the domain at this particular time, there is one large convective event, still actively growing, clearly visible as a large core centered at $(x, y) = (30, 30 \text{ km})$ on the slice taken at 2.6 km. Higher in the atmosphere this core is one unique circular updraft, but at this height the convective downdraft has split the updraft into two distinct components.

On the last panel of Fig. 2, showing vertical velocity at a height of 11 km, it is seen that two convective cores reach the upper troposphere at this point in time, both

with approximate horizontal dimensions of about 3 km in diameter (containing over 50 horizontal grid points).

3. Cold pool characteristics

To focus more on the boundary layer of the initial state, Fig. 3 shows the potential temperature perturbation about the horizontal mean (θ'), the water vapor mass mixing ratio, and surface wind speed for the lowest model level at 50 m, along with the associated surface heat and moisture fluxes. The natural logarithm is used for the surface wind speed and the surface fluxes to prevent the general distribution from being swamped by isolated extreme events. Only a brief examination of the general cold pool characteristics is given here since a more detailed analysis of cold pool statistics will be given in the following sections.

Examining first the temperature field, the convectively generated cold pool is clearly visible as dark circular patches, which are lighter for larger, older cold pools due to the cold pool recovery. The drop in θ in the small new cold pools is typically around 1 K, but reaches as much as 1.3 K at this particular time. The temperature appears to be fairly uniform across even the larger cold pools. The water vapor in the boundary layer also shows the cold pools very clearly. In most cold pools, the depression in boundary layer moisture appears limited, as in observations, although one or two of the larger cold pools show mixing ratio depressions as high as 5 g kg^{-1} . What is remarkable, though, is the clear band of very moist air on the boundaries of the spreading cold pool.

The sensible heat flux reveals large enhancements within the cold pools and is almost perfectly negatively correlated with the boundary layer temperature. One should note that the only way for surface fluxes to alter in this model is through evolving boundary layer characteristics and increased surface wind speeds since the SST is fixed. The domain mean sensible heat flux is 12 W m^{-2} , although outside the cold pool areas the background flux ranges from a minimum of about 3.3 W m^{-2} , but is typically around 7 W m^{-2} . Enhancements within cold pools produce a domain maximum of 65 W m^{-2} , although only a few grid points exceed 30 W m^{-2} . The latent heat fluxes shows a smaller cold pool signature, and the larger older cold pools barely have an impact on surface latent heat fluxes. That said, in newly formed cold pools, the enhancements of the background flux, which ranges from 100 to 150 W m^{-2} (the domain mean is 165 W m^{-2}), produce peak values as high as 600 W m^{-2} . The last panel (Fig. 3e) shows the log of the surface wind speed, indicating maximum surface outflow velocities of about 7 m s^{-1} .

Cold pool evolution

From a single picture it is difficult to appreciate how cold pools trigger new convective activity and how the

convection propagates as a result. Thus Fig. 4 shows the evolution of boundary layer θ' , where each picture is separated by 1.5 h, and the first picture corresponds to Fig. 3 above. To aid the discussion a number of the cold pools have been labeled in each panel. In the first panel for example, three events at B, C, and D have been clearly triggered by the preexisting cold pool originating from convection situated somewhere near A, whose core has dissipated by this point in time, although the anvil cloud is still in existence (not shown). Other clear cases of convective triggering are the cloud F on the edge of the cold pool of E, and H, which resulted from G. Three other cold pools at I, J, and K appear to be isolated, but since they are already of significant horizontal magnitude, it is likely that their "parent" cold pools have already recovered by this stage, an idea that is confirmed by the examination of earlier model fields (not shown). This did not seem to be true for H, whose parent G is still apparent. The reason for this is that cold pool H was associated with two vigorous convective events, and is likely to have grown much more rapidly than I, J, and K.

One and a half hours later, the boundary layer has considerably evolved. The cold pool at A, for example, has recovered and is no longer discernible, and most of the other cold pools have grown substantially. One convective event at L has erupted at a position that was not obviously on a boundary of a cold pool, possibly indicating that cold pool activity is not exclusively necessary to initiate convection. That said, careful examination of Fig. 3b reveals that this point is at the intersection of several lines of high moisture, which are probably remnants of old cold pool events. Two more events, M and N, have also erupted near L, and in fact are seen to occur on the convergence lines where the cold pool of L meets the outflow of events C and D, respectively. The radius of C, D, and L when this event occurs is thus smaller than average (C has a radius of about 8 km for example). This is to be expected, since the dynamical uplifting of air will be greater at the convergence point between two cold pools. The positioning of the new convection reveals that thermodynamical cold pool recovery probably still plays a role, however. Cold pool N does not occur on the straight line intersecting D and L, which would indicate that convection was triggered as soon as the wakes met, but instead occurs to one side. Thus it seems that when the wakes of D and L first collided, the higher dynamical forcing at the smaller radius was unable to initiate convection. This is likely to be due to the thermodynamic recovery of the wake air being inadequate. New convection could also possibly be suppressed by localized atmospheric warming from nearby events, although examination of the temperature field proved this to be unlikely. The same is true for M, which is offset from the line intersecting C and L. At the opposite end of the domain, the vigorosity of H has been proved by the large size its convective wake has reached, with an average diameter

exceeding 30 km. Meanwhile wakes G and K have initiated O at their boundary, and K and A have initiated P at a radius of over 25 km for A.

This emerging pattern of convection almost exclusively triggered by cold pool outflow, often at the intersection between two wakes, is repeated in the third and fourth panels, taken 3 and 4.5 h after the initial picture. For example, the wake from H causes S at its intersection with F; K and E trigger event Q; and R erupts between B and the now almost invisible pool of E. Further examples can be seen in the fourth panel, in which the cold pools of M, N, and L are seen to merge into a large wake, and T is triggered by the almost invisible F and H.

To take a closer look at the triggering of convection, it is useful to be able to demark the cold pool boundaries, a task that is also necessary for the compositing procedure. Since cold pools are essentially density currents, buoyancy (b) is the obvious candidate to use for their identification, which is defined in the standard fashion:

$$b = \frac{g(\theta_\rho - \bar{\theta}_\rho)}{\theta_\rho}. \quad (1)$$

Here g is acceleration due to gravity, the overbar represents the horizontal domain mean, and θ_ρ is the density potential temperature, following the nomenclature of Emanuel (1994), and is defined as

$$\theta_\rho = \theta(1 + 0.608q_v - q_{cl} - q_r), \quad (2)$$

where q_v , q_{cl} , and q_r represent the mass mixing ratios of vapor, cloud condensate, and rain precipitation, respectively. A comparison of the buoyancy and temperature structure of a typical cold pool is conducted in Fig. 5. A vertical slice is taken through two cold pools at different stages of development, passing directly through the center of a newly formed cold pool on the right. Comparing the two fields, it is seen that buoyancy and temperature are similar in structure. Due to the sharp temperature and buoyancy gradient at the cold pool gust fronts, the cold pool lateral dimensions measured at the surface are insensitive to the threshold used. The main differences occur higher in the atmosphere. In particular, the subsaturated downdraft is slightly warmer than the surrounding air, whereas the water-loading effect implies that a negative density temperature perturbation exists as expected. Moreover, the cold pool raised head at the gust front is not always as clearly defined in terms of the temperature as in terms of buoyancy. Many previous numerical investigations have studied individual cold pools initialized artificially, by introducing substantial cold air sources in the boundary layer for example. The large temperature perturbations used, often exceeding 5 K, may be typical of large-scale convective systems, but are probably not appropriate for smaller-scale isolated convective events, which are equally prevalent in the Tropics. Perhaps more important, the cold

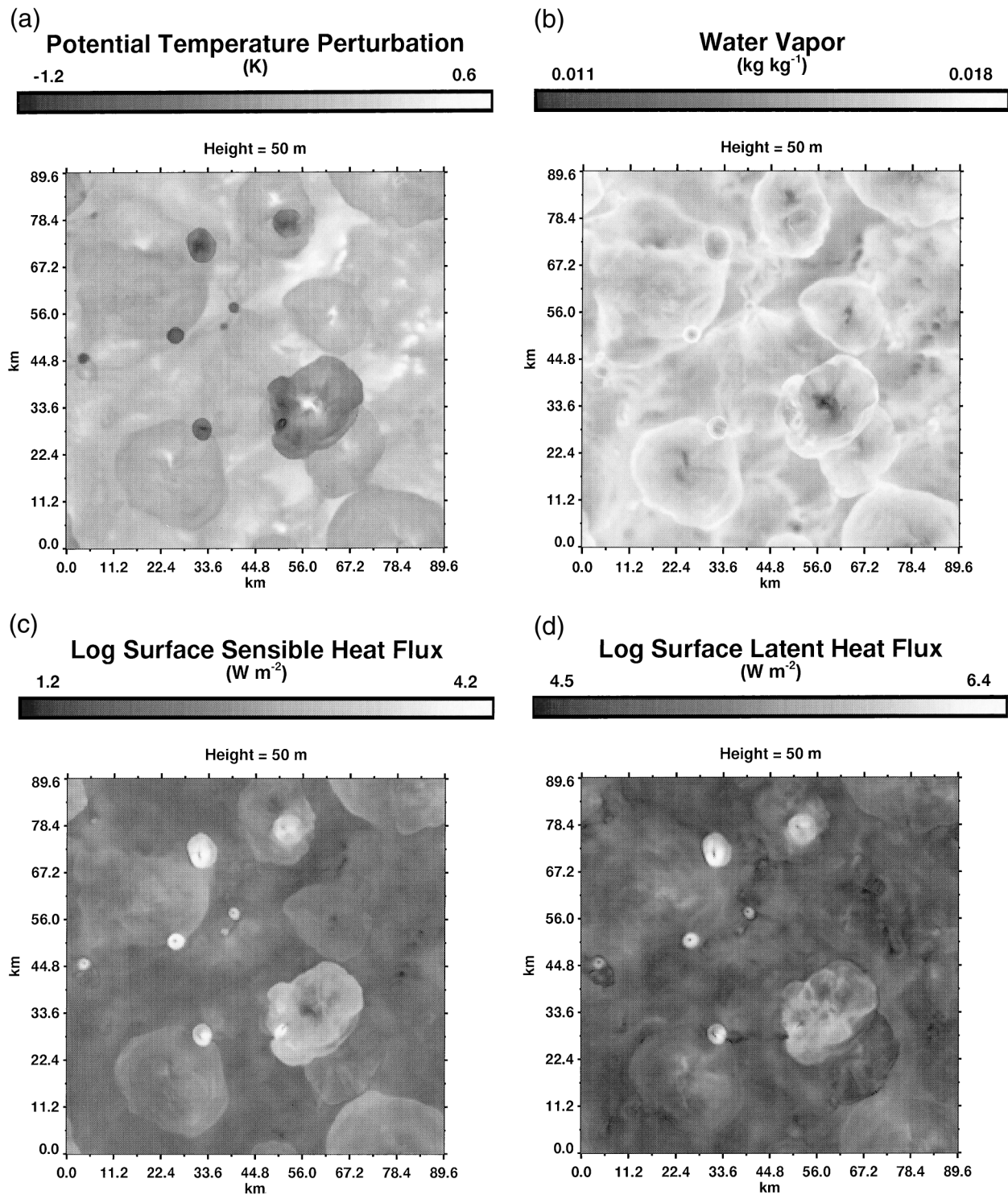


FIG. 3. Slices of (a) potential temperature perturbation about the layer mean, θ' , (b) water vapor mixing ratio, (c) log of the surface sensible heat flux, (d) log of the surface latent heat flux.

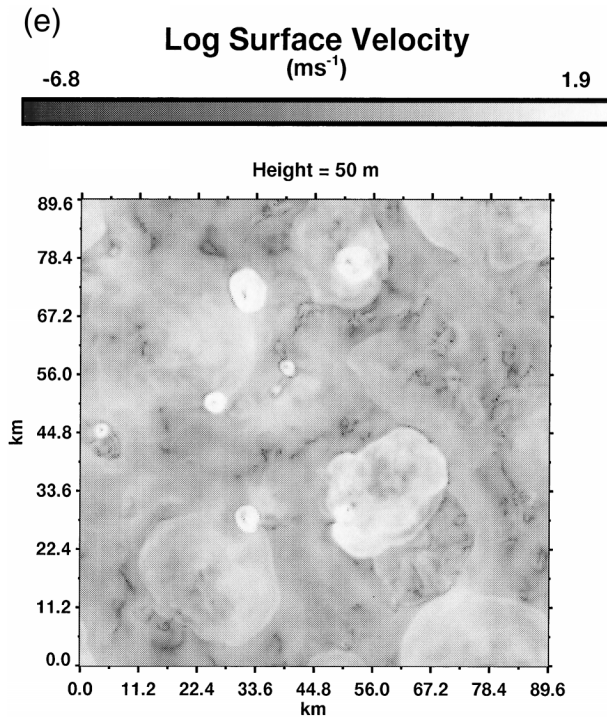


FIG. 3. (Continued) (e) log of the surface velocity, all taken 30 min into the simulation.

pools are often viewed entirely as temperature anomalies, since it is extremely difficult to initialize correctly the water vapor and precipitation fields in the artificial cold pool, and as shown later, the role of the water vapor field is central to the organization of deep convection over the oceans. It is apparent that the characteristics of cold pools can differ considerably when they originate from “realistically” simulated deep convective events. The buoyancy threshold to be used for the identification of the cold pool air is chosen to maximize the cold pool spatial extent. From Fig. 5 it appears that $-0.005 \text{ m}^2 \text{ s}^{-1}$ is a reasonable choice, confirmed by the analysis of a large number of other cold pools (not shown).

Figure 6 shows a series of vertical slices separated by 7.5 min through the same two arbitrary convective events. The shading represents the potential temperature. The thick line marks the $b = -0.005 \text{ m}^2 \text{ s}^{-1}$ contour, demarcating the location of cold pool air. Also shown are the water vapor, cloud areas, and regions of precipitation. In the bottom panel, 525 min into the experiment, two cold pools are apparent, one fairly recently generated cold pool centered at 12 km, and a much older cold pool found between 22 and 30 km approximately, which can be associated with an earlier convective event (not shown). The older cold pool on the right has almost recovered and has minimal temperature anomalies, and indeed the air close to the surface is already excluded from the cold pool mass. In observations it is unlikely that this air would be distin-

guishable from the surrounding air as previously belonging to a cold pool system. On the edges of this cold pool, the contours reveal two peaks where the water vapor mixing ratio exceeds 17 g kg^{-1} . Above the left-hand edge of the cold pool, at $x = 23 \text{ km}$, tiny positive vertical velocities are apparent, with speed less than 0.1 m s^{-1} . Cloud is present just slightly to the left of the cloud pool, the remnants of the ring of arcus-type cloud. At this point in time no convective cell is present, evidenced by the limited vertical velocities. However 7.5 min later these velocities begin to strengthen as an embryonic convective cell begins to develop, until 15 min later, at 547.5 min, a stronger updraft has been established. At this point in time a negative buoyancy perturbation is apparent, but no strong downdraft is in evidence. Over the next 7.5 min the increasing negative buoyancy perturbation is accompanied by a small increase in water vapor, marked by the greater extent of the 17 g kg^{-1} mixing ratio line. Examination of the complete 3D water vapor field shows that this increase is not due to advection perpendicular to the plane viewed, and is not accountable for by surface fluxes, and therefore must be partly due to the wet-bulb process of rain evaporation. The second cold pool mean at $x = 12 \text{ km}$ shows the raised head feature seen in previous studies, with the cold pool spreading more quickly in the easterly direction, presumably due to the nearby convective updraft.

At 562.5 min, the velocity pattern reveals the development of the convective downdraft, which is seen to push the moist, negatively buoyant air to the sides, and inject dry and cold air into the boundary layer. The moist air at the edges of the cold pools is undercut by the drier cold air, often creating a localized vapor maximum, such as the cutoff visible between the heights of 150 and 300 m at $x = 17 \text{ km}$, 555 min into the simulation. However, the dynamics of the flow around the cold pool head remix this moisture back into the gust front region, maintaining the low-level peak in water vapor widely observed in Fig. 3b. The cold pool has thus at this early stage already adopted the structures seen in the horizontal slices, where the negative moisture perturbation is more limited in horizontal extent than the accompanying cold air perturbation. At 570 min the two cold pools are seen to collide. During the following 15 min, the flattening of the buoyancy perturbation above the cold pool at $x = 12 \text{ km}$ and the reduction of the vertical velocities together indicate that the downdraft has expired. The extent of the region experiencing precipitation is also substantially reduced by this time. However, it is interesting to note that the limited downward motion that still exists injects much drier air into the boundary layer in the wake of the downdraft, with mixing ratio values lower than 13 g kg^{-1} observed.

4. Cold pool statistics

a. Analysis procedure

Unlike observation data, where data collection is often restricted to one or two isolated measurement points

Potential Temperature Perturbation (K)

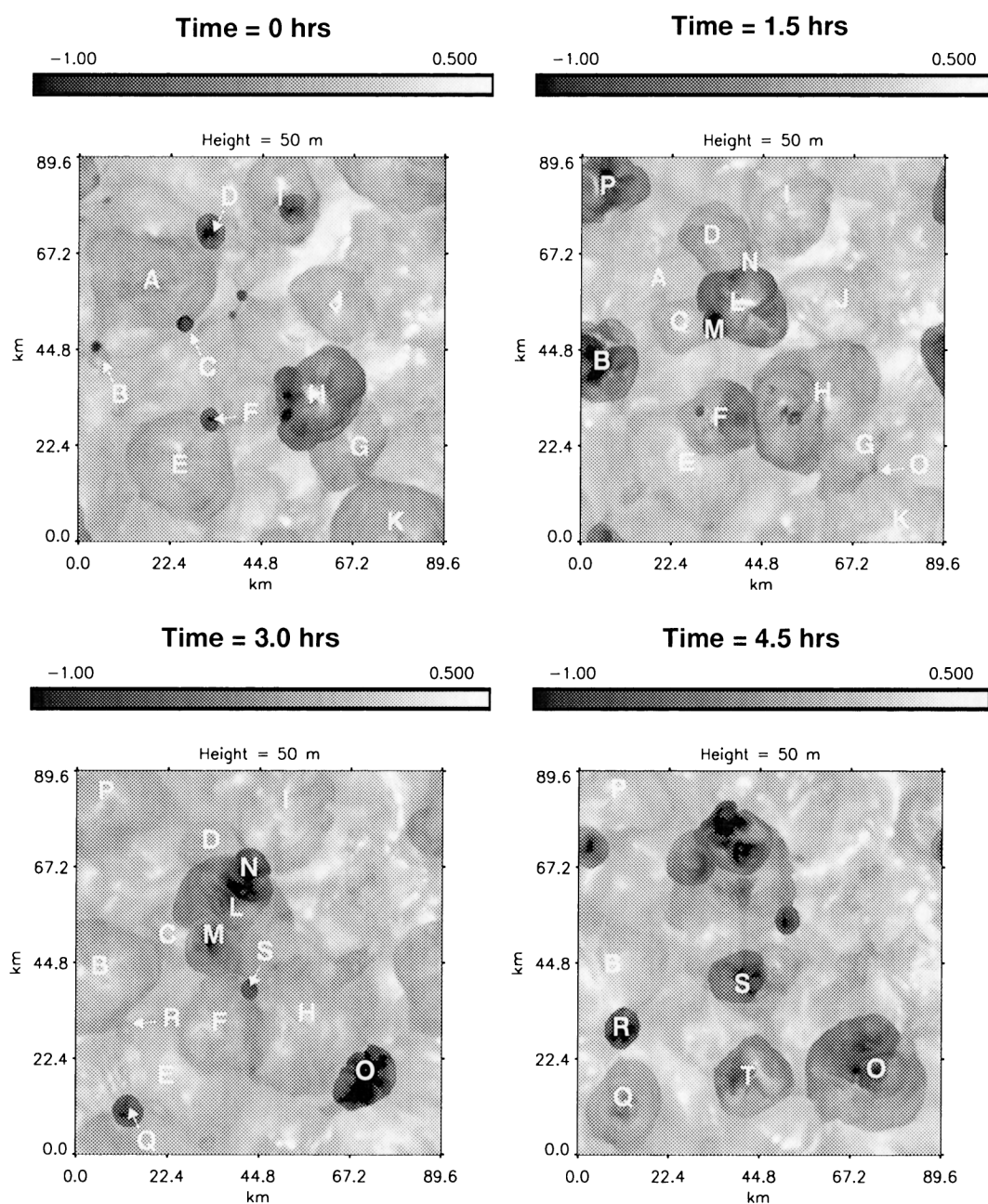


FIG. 4. Snapshots of boundary layer potential temperature perturbation (K), taken 0.5, 2.0, 3.5, and 5 h into the simulation. The plot titles indicate the time elapsed relative to the upper-left panel. See text for details of the cold pool labels.

(e.g., ship collection, tethered balloon), the cloud model can provide a greater depth of information, and therefore more possibilities for collecting the cold pool statistics. For example, it is possible to examine a line through the cold pool at a given height at various times in the cold pool evolution, imitating the data that would be provided by an aircraft making repeated passes (at infinite speed) through the cold pool. As an example, Fig.

7 shows the development of the cold pool marked “B” in Fig. 4 in terms of the water vapor, θ' , horizontal and vertical velocities, surface rainfall, and surface fluxes, in addition to the derived quantities of moist static energy (h) and buoyancy. All data except the surface quantities and vertical velocity are shown for the bottom model level at 50 m; the vertical velocity is for an altitude of 100 m. The slices are taken in an east-west

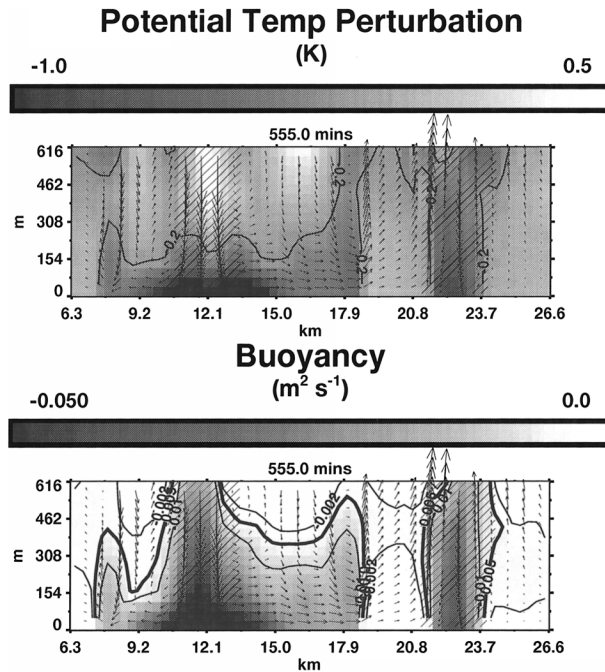


FIG. 5. Vertical slice taken through two arbitrary cold pools at 555 min into the simulation. The shading of the upper panel shows θ' using a contour value of -0.2 K, and shows the lower panel buoyancy b , as described in the text, with contours marking buoyancies of -0.01 , -0.005 (thick line), and -0.002 $\text{m}^2 \text{s}^{-1}$. The diagonal lines indicate areas where the rain mass mixing ratio exceeds 0.1 g kg^{-1} , and the arrows represent the flow field.

direction and show the prewake conditions and the development after 30, 60, and 90 min respectively. The graphs for 30 min (dotted lines), which correspond to the time at which Fig. 3 is taken, show clearly the signal of the new downdraft. The vertical velocity, for example, peaks at about -1.4 m s^{-1} and surface velocities are enhanced over a distance exceeding 3 km with a maximum of 4 m s^{-1} . Rainfall is strong at this time, exceeding 100 mm h^{-1} . It is interesting to note that although the potential temperature has been clearly depressed by more than 1 K, the water vapor shows no signs of any decrease and has, in fact, actually increased in value, as seen in the previous section. The increased surface wind speed causes an enhancement of both the sensible and latent surface heat fluxes, with a much larger percentage increase in sensible heat flux, as previously noted in the observational studies, due to the addition increase in the air–sea surface temperature difference.

Half an hour later (dashed lines) the θ graph shows that the wake has spread to a diameter of almost 10 km, with the negative perturbation reaching -1.4 K. The horizontal velocity actually shows the highest velocities near the edges of the cold pool, with values exceeding 5 m s^{-1} , and in association with this the vertical velocity shows considerable uplift at the cold pool edges, with an upward velocity of more than 0.5 m s^{-1} on the west-

ern edge. By this time, the water vapor now also shows a significant depression, dropping by around 2 g kg^{-1} . The depression is seen to be more restricted in horizontal scope than that of θ and toward the edges of the wake the vapor appears to in fact be slightly greater than the surrounding environment. The dot–dashed lines on these figures, showing the wake state after 90 min, indicate that the convective downdraft that initiated the wake has expired, as one would expect. The potential temperature in the center of the wake has recovered rapidly to the prewake conditions, whereas the water vapor here has fallen even lower to a very dry 11 g kg^{-1} . This indicates that the central temperature recovery is not due to surface fluxes, but is instead due to environmental air from above the boundary layer being drawn down in the wake of the dying downdraft. The moisture perturbation is sufficient to maintain a significant negative buoyancy perturbation throughout the central region of the wake. The rainfall rate associated with this system has fallen to around 5 mm h^{-1} associated with the anvil cloud, which, due to the lack of mean background vertical wind shear, is restricted in horizontal extent to around 6 km in diameter. The surface velocity away from the center of the cold pool is largely above 3 m s^{-1} and thus both the sensible and latent surface heat fluxes remain enhanced.

Examining slices through cold pools has the advantage that the exact values for the cold pool quantities are seen, but it is sometimes more difficult to see general characteristics. Since there is no background mean wind in this experiment, the cold pools are not advected significantly horizontally, and grow almost perfectly circular in form. Thus it is also possible to examine the cold pool statistics by binning the cold pool data by its radius from the cold pool center. This has the advantage that the averaging will more clearly show general characteristics of the cold pool, but also has the disadvantage that the statistics can become contaminated by other newly developing cold pools, and that the cold pool features can become smeared out by the averaging process, especially if the cold pool is not exactly circular in shape.

As an example of this, the first three times of Fig. 7 are repeated in Fig. 8 as radially calculated statistics. The general characteristics are seen to be the same in both plots, but the radially calculated values show much more clearly the peak in water vapor content inside the wake's gust front, and the statistics are seen to be smoother. However, the averaging process reduces the peak values of the statistics and also makes the transition between the wake and the environmental air much less sharp and well defined.

A third possible way of collecting cold pool statistics would be to define a criterion for a grid point to be considered as cold pool air, a certain minimum negative buoyancy for example, and then starting from the manually defined cold pool center, collect statistics from all connecting points that fulfill this cold pool criterion.

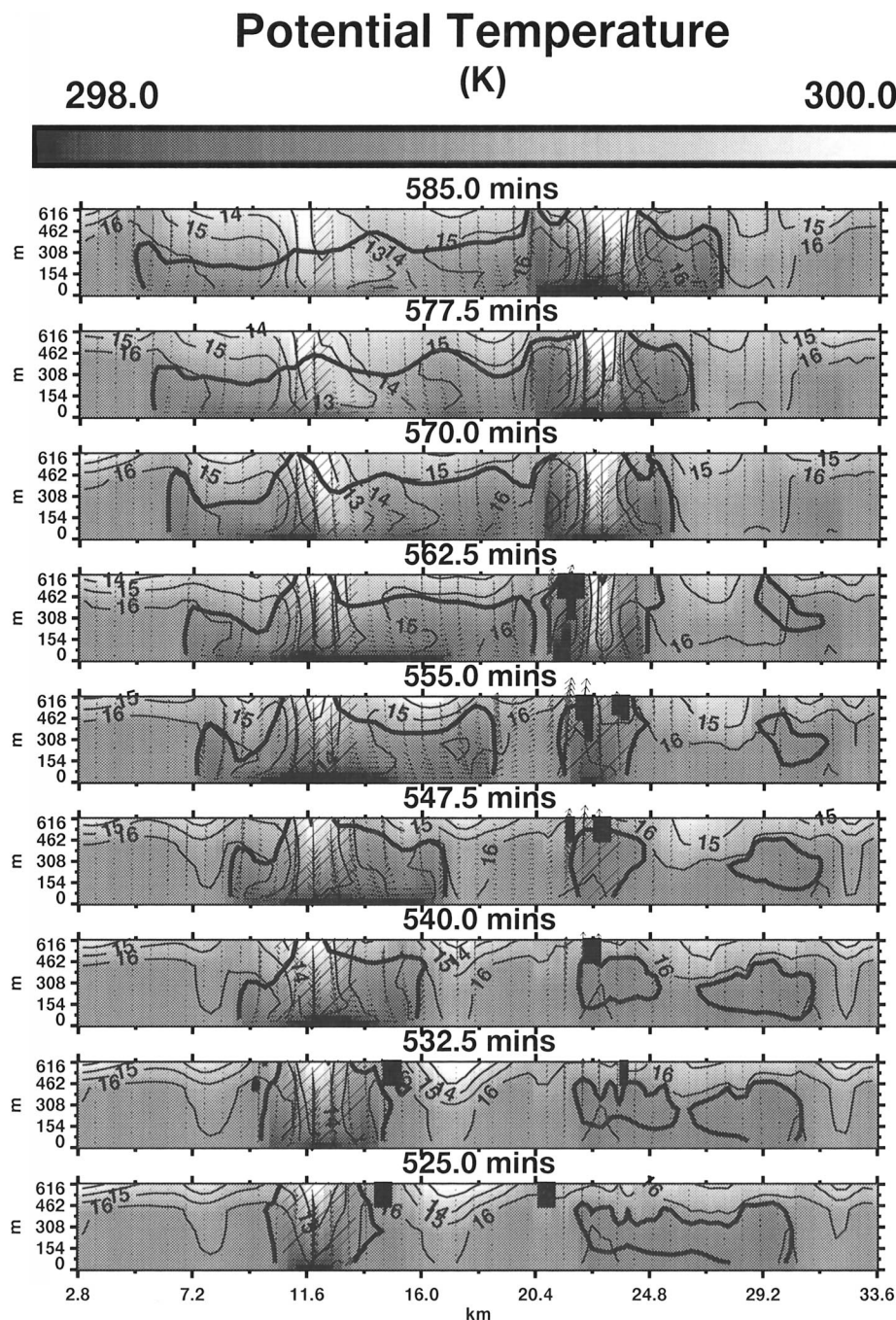


FIG. 6. Vertical slices separated by 7.5 min taken through two arbitrary cold pools. The shading represents θ , with the thick contour marking the $b = -0.005 \text{ m}^2 \text{ s}^{-1}$ line to indicate cold pool air. The contours represent water vapor mixing ratios of 13, 14, 15, 16, and 17 g kg^{-1} . The arrows represent the flow field, with the maximum arrow length representing a velocity of 7 m s^{-1} . Also marked are the regions of precipitation (as for Fig. 5), and the blacked out squares indicate regions where the cloud amount also exceeds 0.1 g kg^{-1} .

This would have the advantage that a noncircular cold pool would not smear the statistics, and that a mean cold pool radius could be more accurately defined. However, attempts to use this method showed that it was difficult to avoid the statistics becoming severely contaminated

by adjacent cold pools, and so this method was not used in this paper.

For the compositing procedure a total of 67 cold pools were manually selected whose birth and complete recovery occurred during the 24-h period. Both the line

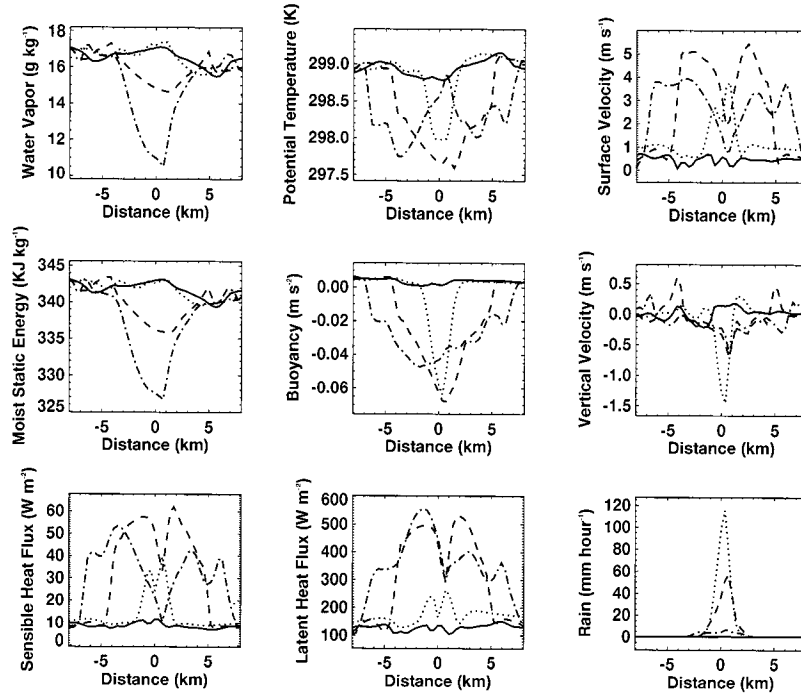


FIG. 7. Cross sections at various times through cold pool B in Fig. 4 for the water vapor mass mixing ratio (g kg^{-1}), potential temperature (K), horizontal velocity (m s^{-1}), moist static energy (KJ kg^{-1}), buoyancy (m s^{-2}), vertical velocity (m s^{-1}), latent heat flux (W m^{-2}), sensible heat flux (W m^{-2}), and rain rate (mm h^{-1}). The solid, dotted, dashed, and dot-dash lines show the cross section at 0, 30, 60, and 90 min into the simulation. The solid line thus shows the “prestorm” state, and the dotted line corresponds to the first panel in Fig. 4.

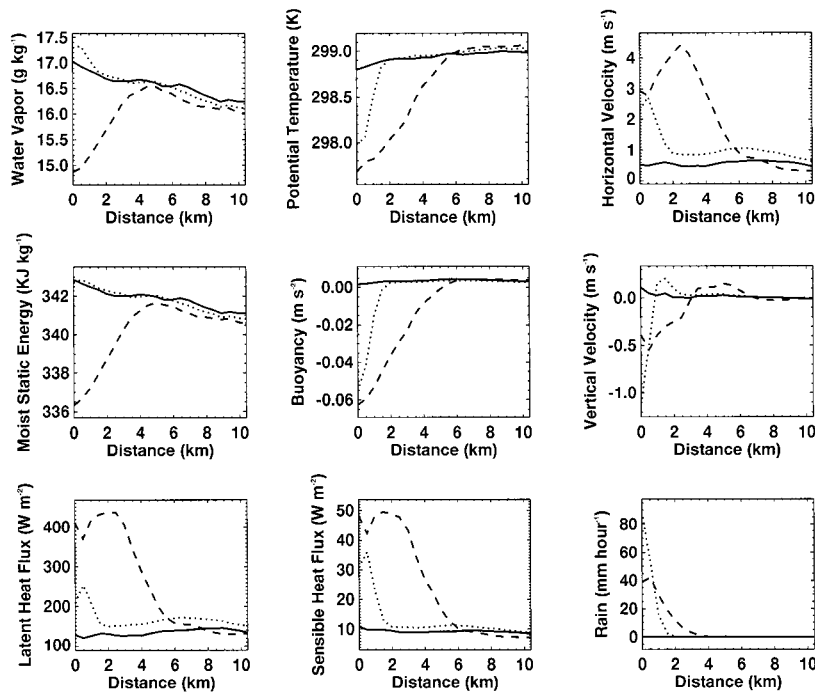


FIG. 8. As for Fig. 4, but calculating the statistics radially (see text for details), and only showing the statistics for 0 (solid), 30 (dotted), and 60 (dashed) min into the simulation for clarity.

TABLE 1. Cold pool statistics using 1D compositing method.

	Mean, min $\Delta\theta$ (K)	Mean, min Δq (g kg ⁻¹)	Mean, max latent flux (W m ⁻²)	Mean, max sensible flux (W m ⁻²)	Mean, max horizontal wind (m s ⁻¹)
Wake mean	-0.55, -1.0	-0.65, -1.5	320, 470	31, 51	2.6, 4.8
Wake center	-0.70, -1.3	-1.3, -2.6	340, 540	33, 60	2.5, 5.1
Wake gust	-0.56, -0.80	+0.25, -0.21	310, 400	33, 17	3.1, 4.5
Wake min, max	-0.93, -1.7 (min)	-2.2, -3.9 (min)	430, 670 (max)	44, 76 (max)	3.9, 6.8 (max)

and radial compositing methods outlined above were used, referred to later as the “1D” and “2D” compositing methods, respectively. For each cold pool the center point was calculated for the first time at which the cold pool is apparent, which was assumed to remain fixed with time, since no background wind is present in this experiment. For the 1D slice compositing method a direction was also selected for each cold pool from four choices of east–west, north–south, and the two diagonal directions. The direction chosen attempted to avoid other cold pools developing in close proximity at later times, in an attempt to minimize the corruption of the cold pool statistics. The slices are always taken through this central point.

The actual compositing method follows that of Young et al. (1995) closely. The model fields were analyzed every 7.5 min; the data for each cold pool are allocated to a number of bins using linear interpolation; and the time allocated to the bins in the final composites is calculated from the average duration of all the cold pools examined. Young et al. (1995) rejected cold pools lasting less than 6 h, but the cold pools associated with the isolated collective events here have much shorter life spans. Instead, we choose to filter out the smaller cold pools associated with midlevel or smaller convective events by rejecting all cold pools that do not attain a radius exceeding 5 km. This left a total of 61 analyzed cold pools with both compositing methods.

The cold pools are defined to “exist” if the buoyancy of all the points lying within a certain radius of the center point is less than the threshold buoyancy of $-0.005 \text{ m}^2 \text{ s}^{-1}$. In 1D, a radius of $1.5 \times dx = 525 \text{ m}$ was used (three grid points examined), and in 2D the radius was set to $\sqrt{2}dx = 495 \text{ m}$ (five grid points examined). The general evolution of the cold pool properties was found to be insensitive to the threshold chosen. Using $b < -0.005 \text{ m}^2 \text{ s}^{-1}$ resulted in a wake lifetime of about 2.5 h, which compares well with the 3.5-h recovery time in observations of 9 submesoscale convective system nonlinear events by Saxen and Rutledge (1998). Gaynor and Ropelewski (1979) reported a total wake lifetime of 2.9 h for cold pools in GATE, but this figure is increased by the inclusion of cold pools associated with squall line systems that had wake lifetimes exceeding 16 h. Thus the recovery time for isolated convective events in low wind shear environments is likely to lie even closer to the model result.

Young et al. (1995) defined two criteria for the ter-

mination of cold pools: the recovery of the boundary layer temperature to the SST value, or a drop in the 5-h running mean temperature indicating that other processes are dominating the boundary layer budget. In these simulations, such a reduction would be caused by the emergence of a newer cold pool nearby the one analyzed. However, since the cold pools here were “handpicked” in an attempt to limit this, the majority of cold pools analyzed exhibited full boundary layer recovery, especially with the 1D compositing technique.

b. Cold pool statistics

The statistics from each processed cold pool are shown in Table 1, where the 1D compositing method outlined above was used. The columns across the table show the (temporal) mean and minimum or maximum values of the θ and water vapor perturbations, the latent and sensible heat fluxes, and the horizontal velocity, respectively. The rows indicate the spatial averaging used, with the first row giving the mean value averaged across the whole cold pool. The second and third rows give the central and gust front values, where for the cold pool “center” the spatial averaging is performed across the central third of the cold pool. For the gust front diagnostic, the outer third of the buoyancy defined wake is averaged, thus following the wake front in a pseudo-Lagrangian fashion. The statistics for the gust front are restricted to the period between the initial cold pool detection and the time at which the maximum radius is achieved, since after this time, the recovery of the outer edges of the cold pool corrupts the gust front statistics. The final row indicates the minimum or maximum value found anywhere within the cold pool at any particular time.

The values in the table appear to agree reasonably well with observational studies, providing one takes into account the type of convective organization. For example, the mean cold pool θ depression peaks at a value of 1.0 K, which seems small compared to the 4 K maximum observed by Johnson and Nicholls (1983) in a GATE squall line, the 2 K noted by Geldmeier and Barnes (1997) in the study of an MCS, and the 2 K mean peak perturbation reported by Young et al. (1995) of 42 wakes exceeding 6 h in lifespan during the Tropical Ocean Global Atmosphere Coupled Ocean–Atmosphere Response Experiment (TOGA COARE). However, this is to be expected since these large organized

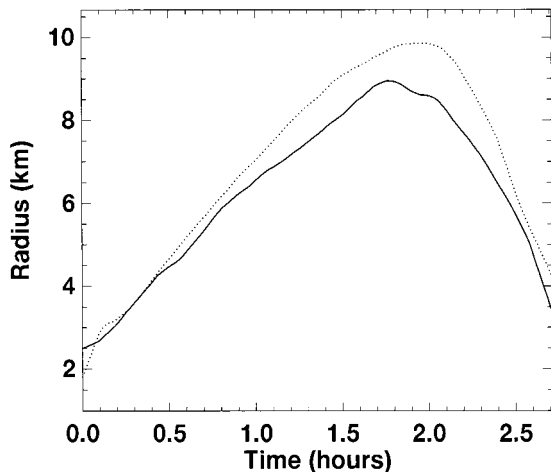


FIG. 9. Composite cold pool radius as a function of time. The solid line shows the 1D composite value and the dashed line shows the corresponding 2D calculation.

convective systems have been shown to produce deeper wake temperature depressions (Saxen and Rutledge 1998). The fact that the model statistics only includes those cold pools clearly associated with a single convective event is very likely to be the reason for the lower value compared to other observations that included a wider range of convective types, such as Gaynor and Ropelewski (1979), 1.3 K; Barnes and Garstang (1982), 2 K (1.2 K mean depression); Addis et al. (1984), 1.9 K; and Saxen and Rutledge (1998), 2 K (for nonlinear unorganized convection, named SM–NL). Wakes that were contributed to by more than one convective event were ignored in the model compositing, since the merging of two wakes, or the additional input from convection occurring within the wake area, would mean that other processes could dominate the wake recovery processes that we wish to analyze (Young et al. 1995). However, it was exactly these cold pools that produced the largest temperature and moisture perturbations. The largest θ depression observed at any time or position within one of the composited cold pools was 1.7 K, but some cold pools resulting from multiple convective events had perturbations approaching 3 K. In comparison, maximum depression of the spatial mean water vapor at 1.5 g kg^{-1} is more in line with observations, which show a larger range of values, ranging from 0.1 g kg^{-1} (Addis et al. 1984) to 3 g kg^{-1} (Johnson and Nicholls 1983) for example.

The cold pool spatial and temporal mean latent and sensible heat surface fluxes attain values of 320 and 31 W m^{-2} , respectively. Given the mean values of 165 and 12 W m^{-2} , wakes enhance latent and sensible fluxes by a factor of approximately 1.9 and 2.6, respectively. The peak flux enhancement of the cold pool mean is substantially larger, with an amplification factor of 2.8 and 4.3 for the latent and sensible heat fluxes. These enhancement factors compare well to the observations of

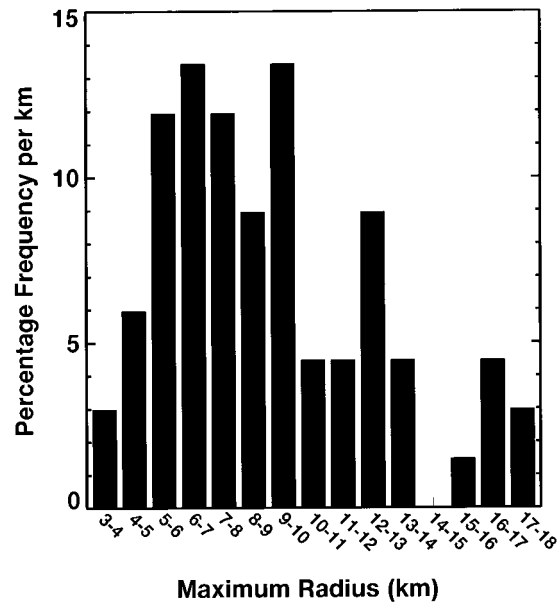


FIG. 10. Histogram of the maximum radius achieved by all 67 cold pools.

Johnson and Nicholls (1983) (2 and 5), Young et al. (1995) (1.5 and 2.0, and 3 and 4, respectively, for two cruises), Jabouille et al. (1996) (2 and 3), and Saxen and Rutledge (1998) (2 and 4 for SM–NL), especially bearing in mind the differences in temperature drop and convective organization remarked on above. This is probably partially the result of a good representation of the wind speed mean increase of 2.6 m s^{-1} , which appears in good agreement with Addis et al. (1984) (also 2.6 m s^{-1}), and Saxen and Rutledge (1998) (2 m s^{-1} for SM–NL). Table 1 also reveals the substantial difference between the center and gust areas of the cold pools, especially in the water vapor perturbation. In stark contrast to the center of the wakes, the gust area has a mean positive perturbation of 0.25 g kg^{-1} , meaning that the cold pool air at the edges is always more moist than the surrounding environmental air.

c. Cold pool composites

The first composite graph shows the radius as a function of time (Fig. 9), and shows similar results with the two compositing methods. The radius of the cold pool when detected has an average of around 2 km, on the order of the downdraft core size. This grows almost linearly to a maximum of around 8 to 9 km after 2 h, after which the cold pool decays in size. This maximum does not appear to be very large when compared to the model snapshots. This is an artifact of the compositing procedure, since the cold pools take different amounts of time to reach the maximum radius, and thus the compositing procedure strongly smooths the profiles and gives a maximum radius smaller than the mean of the peak value of each individual wake profile (also noted

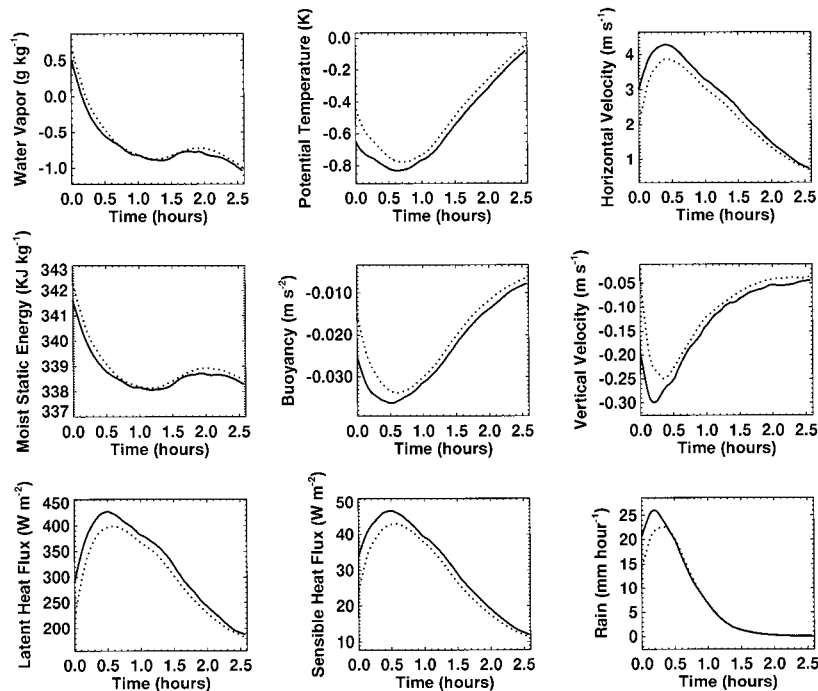


FIG. 11. Composites of the mean cold pool water vapor perturbation from boundary layer mean (g kg^{-1}), potential temperature perturbation (K), horizontal velocity (m s^{-1}), moist static energy (kJ kg^{-1}), buoyancy (m s^{-2}), vertical velocity (m s^{-1}), latent heat flux (W m^{-2}), sensible heat flux (W m^{-2}), and rain rate (mm h^{-1}) calculated for the 61 wakes exceeding 5 km in radius. The solid lines show the composite value calculated using the 1D technique, the dashed lines the 2D radial compositing technique. See text for details.

by Saxon and Rutledge 1998). The distribution of the maximum cold pool radius attained (analyzing all 67 cold pools) reveals (Fig. 10) that the majority of the cold pools attain a maximum radius between 5 and 10 km, but that larger radii are not uncommon. The mean radius obtained is 8.6 km. The largest radius attained by any cold pool was approximately 18 km, but again, cold pools resulting from multiple convective events achieved radii as great as 30 km on occasions.

The composite data for the cold pool mean statistics (Fig. 11) reveal predictable behavior for many of the model fields, and also that the line and radial compositing methods give very similar results. For the majority of the fields, the cold pool statistics appear to peak approximately 30 min after the cold pool is first detected, followed by a recovery period of around 2 h. The composite mean potential temperature attains a minimum of around 0.8 K below the boundary layer mean of 298.9 K. The mean surface velocity perturbation peaks at around 4 m s^{-1} , and the surface latent and sensible fluxes reach peak values of 400 and 45 W m^{-2} , respectively. The variable that reveals the most surprising behavior is the cold pool water vapor content. As observed in the individual cold pool example examined earlier, the water vapor starts at a value close to, but around 0.5 g kg^{-1} moister than, the boundary mean of 16.2 g kg^{-1} , and reaches its minimum value

at a later time than the other model variables at about 1.5 h after the cold pool is detected. After this point the water vapor begins to recover a little, but drops off again at the end of the cold pool life span. The tailing off during the last 30 min of the composite cold pool is due to the outer edges of the cold pool “recovering” and is therefore no longer included in the statistics (i.e., the cold pool is decreasing in size), and thus is absent if statistics are compiled to the point of the cold pool radial maximum (not shown). The lag in water vapor depression and the subsequent nonrecovery of the cold pool water vapor were also seen in the observations of Young et al. (1995). Further examination of Fig. 11 shows, as one would expect in the boundary layer, that the moist static energy closely follows the water vapor content of the boundary layer, while the buoyancy closely matches the temperature profile.

Figure 12 shows the composites for water vapor, θ , moist static energy, and buoyancy at the center of the cold pool. The behavior is similar to the cold pool mean values except that the temperature and moisture depressions are much greater, and that the water vapor shows a clearer partial recovery in the later stages of the cold pool development. This contrasts strongly with the cold pool statistics just inside the gust front, composited in Fig. 13. As already hinted at by the snapshots of the boundary layer, the water vapor in the outer 30%

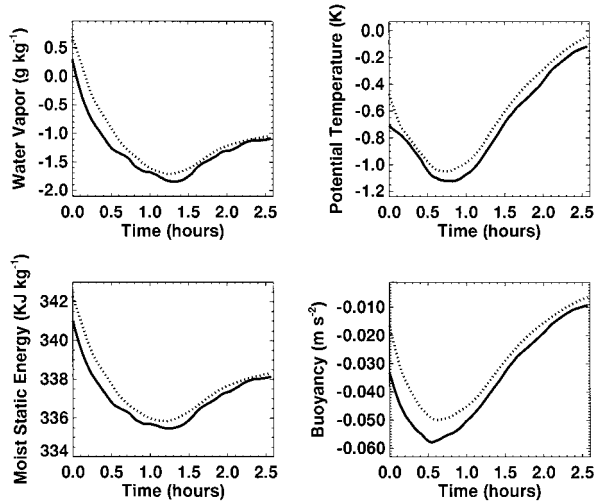


FIG. 12. As Fig. 11 but calculated for the wake centers.

of the (buoyancy defined) cold pool is always moister than the boundary layer mean. After the initial 30 min, the water vapor perturbation remains constant at about 0.2 g kg^{-1} .

Figure 13 thus confirms that the high vapor contents on the edge of cold pools, and the associated high values of CAPE observed by Tompkins (2001), are in fact not the result of recovery through surface fluxes, but are the product of a more complicated process, produced schematically in Fig. 14. The air that seeds cumulus clouds is already by definition moister than average,

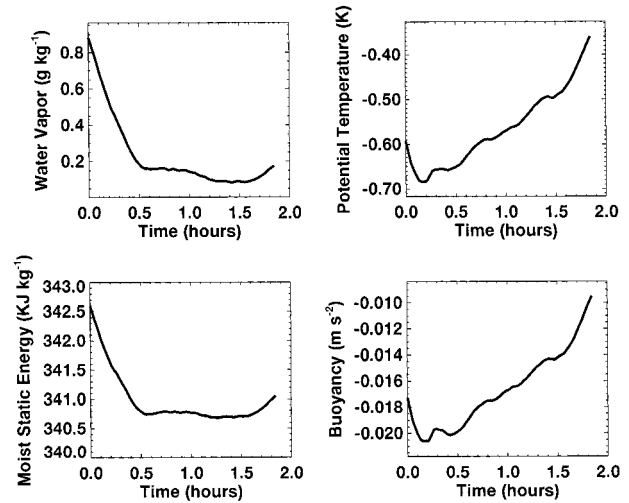


FIG. 13. As Fig. 11 but calculated for the points corresponding to the last 33% of the wake radius lying inside the gust front, using the 1D compositing technique. The composite is here calculated between the time of cold pool detection and the time at which the maximum radius is achieved (i.e., decaying phase ignored). The 44 wakes that require at least 1 h to achieve their respective maximum radii are composited.

with higher θ_e values, as already seen in TOGA COARE observations (Kingsmill and Houze 1999). The boundary layer below convection is moistened and cooled by the evaporation of precipitation, before the convective downdraft itself reaches the boundary layer, exactly as observed by Betts (1984). This explains the apparent

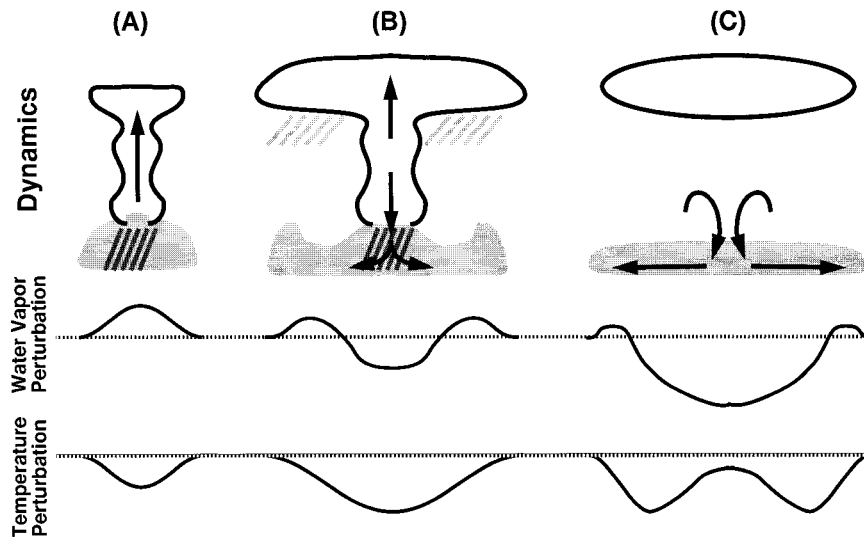


FIG. 14. Schematic diagram of cold pool development. (A) A deep convective tower develops, moistening and cooling the subcloud layer through the evaporation of rainfall, air that already had high θ_e values. (B) As convective tower matures, downdrafts introduce cold, dry air into the boundary layer, and the moist band is advected at the edges of the newly formed cold pool. (C) Convective system dissipates, leaving cirrus remnants. The edges of the cold pool have already recovered in temperature due to the action of surface fluxes, and are able to trigger new convection. In the wake of the downdraft, environmental air is entrained into the boundary layer, causing the fast recovery of the temperature to prewake conditions, but increasing the moisture perturbation.

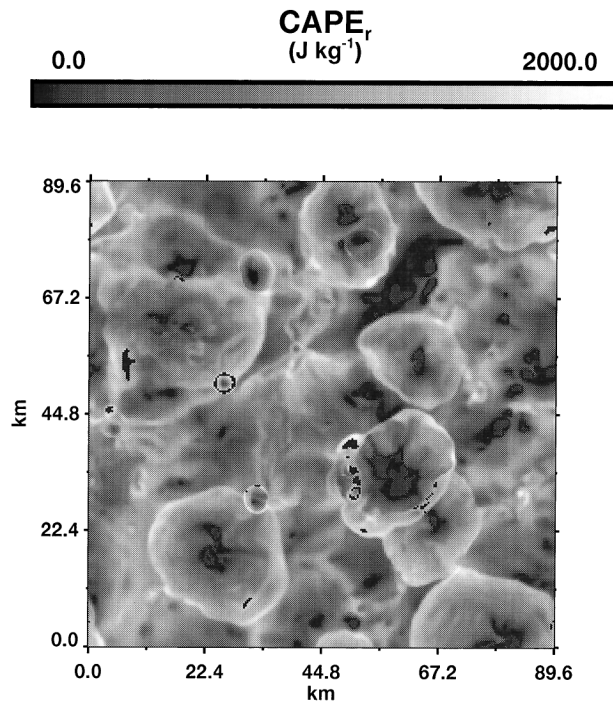


FIG. 15. Snapshot of reversibly calculated CAPE, taken 30 min into the simulation.

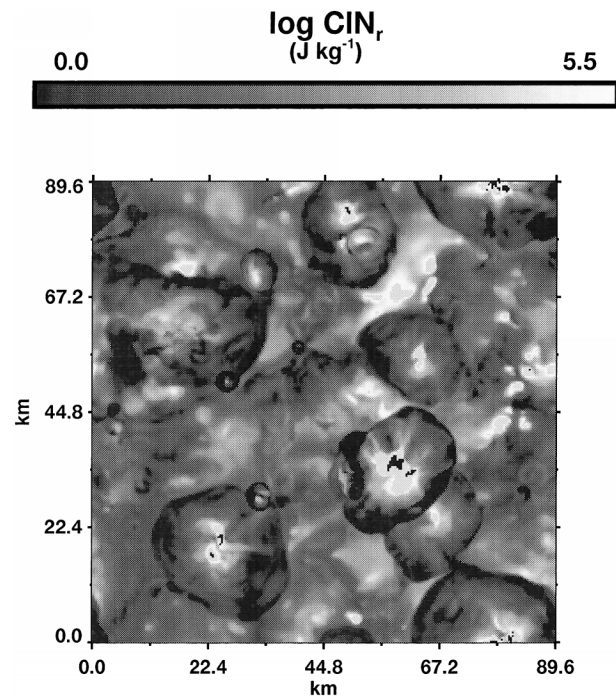


FIG. 16. Snapshot of reversibly calculated CIN, taken 30 min into the simulation.

lag between the cooling and moistening peak observed both here and in observations. This wet-bulb evaporation process does not affect the θ_e of the air, but does introduce a negative buoyancy perturbation. This negatively buoyant air is then pushed out on the edges of the following downdraft, which injects cold dry air of a much lower buoyancy into the boundary layer. Since both air masses are negatively buoyant they are collectively identified as convective wake air, but the marked difference in the water vapor profiles of Figs. 12 and 13 reveals their different respective histories. The examination of individual cold pool events revealed that this cold, dry air tends to undercut the moister air at the gust front, but that the dynamical circulation around the wake head maintains the general water vapor structure and the two distinct moist and dry cold pool regions.

Surface fluxes, enhanced by increased surface winds and larger surface–boundary layer differences, act to increase the wake’s temperature and moisture content, but turbulent entrainment of air from above the boundary layer roughly cancels this for water vapor at the gust front, while enhancing the recovery of temperature. As the temperature depression recovers, CIN reduces. At the same time, the positive water vapor perturbations mean that the parcel has to be lifted through a smaller distance to reach its Lifting condensation level. Eventually CIN will almost be removed and any small uplift of the gust front boundary layer air can trigger new convection, which will preferably occur at these locations due to the presence of large CAPE values. The

collision of a cold pool with another wake, even at very small horizontal velocities at the point when the wakes have almost recovered, is enough to provide the necessary uplift, and will generate convection at smaller radii. Note that since the cold pool air itself is the source for new convection, this mechanism for initiating deep tropical convection is different from that observed by Fankhauser et al. (1995) and Kingsmill (1995), who noted that convection was triggered ahead of colliding cold pool air (or sea breeze front) air in a similar fashion to that noted in squall lines system propagation. These studies were conducted over land in situations with vigorous wakes.

To illustrate the spatial distribution of CAPE and CIN with respect to cold pool activity, Figs. 15 and 16 show these quantities for the model field 30 min into the simulation, the same point in time as the earlier snapshots. As seen in Tompkins (2001), the highest CAPE values in the domain are very clearly associated with the outer regions of the cold pools. At the same time, while the majority of the cold pool regions are associated with significant CIN, the CIN is observed to reduce to almost zero moving toward the edges of the wakes, exactly in the places where the largest CAPE values are found.

5. Discussion

Here we briefly examine the general evidence in observational studies for the triggering mechanism found in the numerical investigation. First, it should be noted that the mechanism suggested here for deep convection

would be difficult to identify directly in observations since, at the point the new convection is spawned, the temperature perturbation is limited in magnitude and difficult to associate with previous cold pool activity. However, in possible support of the mechanism, it is interesting to note that both Young et al. (1995) and Saxen and Rutledge (1998) observed that the mean wake in their studies exhibited almost complete recovery in temperature to prewake conditions, despite the fact that the advent of new convective activity was reported to have terminated the compositing of many cold pools (i.e., the boundary layer temperature begins to fall before recovery is complete). This therefore implies that in the cases where cold pools initiate new convection, this event must have usually occurred when the cold pool was already mature and had almost recovered in temperature, rather than substantially before.

In addition, many other cold pool characteristics identified in this study are easier to verify from field experiments. Observations of the moistening and cooling of the in situ boundary layer air by evaporation of precipitation in the vicinity of convection were made by Betts (1984). Increases in water vapor by as much as 3 g kg^{-1} were noted, prior to the development of the downdraft and associated cold pool, exactly as seen in the CRM simulation. Young et al. (1995) documented the longer delay in the onset of the dry vapor perturbation. In their studies, both Geldmeier and Barnes (1997) and Johnson and Nicholls (1983) identified the smaller spatial extent of the water vapor depression relative to the temperature signal. In other words, the periphery of the wakes in their studies had vapor amounts equal (or exceeding) the background environmental values, just as has been noted here. Furthermore, Johnson and Nicholls (1983) emphasized in particular the significant time delay in the onset of the water vapor depression, which was also noted by Zipser (1977), and also highlighted the role of entrainment for the fast recovery of temperature. Perhaps the best example of observations confirming these model findings is the investigation of Addis et al. (1984), who showed water vapor increasing significantly on the passage of a cold pool gust front, which they identified with a mature front. They also note that in cases where the cold pool was drier than the environmental value, that the dryness occurs a long way behind the front.

With the knowledge gained from this numerical investigation, it now becomes clear why the behavior of the water vapor fields varies substantially between cold pools in observational studies. The variability is not only due to contrasting attributes of the respective parent convective towers, but also to the position the observation has taken relative to the convection. If the cold pool is sampled near the deep convective downdraft, the entire history of the cold pool is observed. The measurements will reveal the onset of a dry perturbation at around the same time as, or perhaps later than, the occurrence of the temperature anomaly, with the mois-

ture taking longer to recover. Exactly these features are seen in an example cold pool (Fig. 17) observed during the TOGA campaign. The data are from Young et al. (1995) and the reader should refer to this paper for details of the observation techniques. Since cold pools are more likely to be identified if they are sampled near their source, these features are also reflected in the cold pool composites of Young et al. (1995). On the other hand, if the measurement is taken farther from the convective tower, the cold pool is only sampled at its extremities, and only during its mature phase. As noted in the observations of a mature cold pool by Addis et al. (1984), in these cases the temperature drop at the gust front is not accompanied by any clear water vapor signature, or indeed the water vapor may even increase on the passage of the front, as shown in the example in Fig. 18. In order to emphasize how the CRM can reveal this behavior, Fig. 19 shows a cold pool measured in four different locations of differing distances from the cold pool center. The plot clearly shows how a ship taking measurements near the convective tower would measure a sharp fall in boundary moisture as the cold pool passes, with a delayed recovery with respect to the temperature. On the other hand, if the ship sampled the *same* cold pool a distance of 5.25 km away, it would instead note a small increase in humidity on the passage of the front.

6. Conclusions

The large-scale circulation in the Tropics is intimately tied to the organization of tropical deep convection, and thus it is crucial to understand the factors that control this organization. Even in the absence of large-scale wind shear or SST gradients, it is possible that other feedback mechanisms can act to spontaneously organize tropical deep convection. Tompkins and Craig (1998), for example, used a 3D cloud-resolving model to show that interactions between radiation and convection could act to strongly localize convection. Tompkins (2001) followed from this study, and revealed that even if the radiative-convective interactions were removed, deep convection still organized into mesoscale clusters on the order of 200 km in lateral extent, separated by clear regions in which convection was suppressed. The interaction between convection and the water vapor field was found to be responsible for the formation of the convective clusters, but it was noted that cold pool activity initiated new deep convective cells at their boundaries. It is this role of cold pools that has been investigated further in this paper.

Cloud-resolving model experiments were conducted to document the evolution of cold pools produced by deep convection in the situation of limited large-scale wind shear. Ignoring the cold pools resulting from multiple deep convective events, the mean model cold pool attained a minimum temperature and water vapor mixing ratio depression of 1 K and 1.5 g kg^{-1} , respectively,

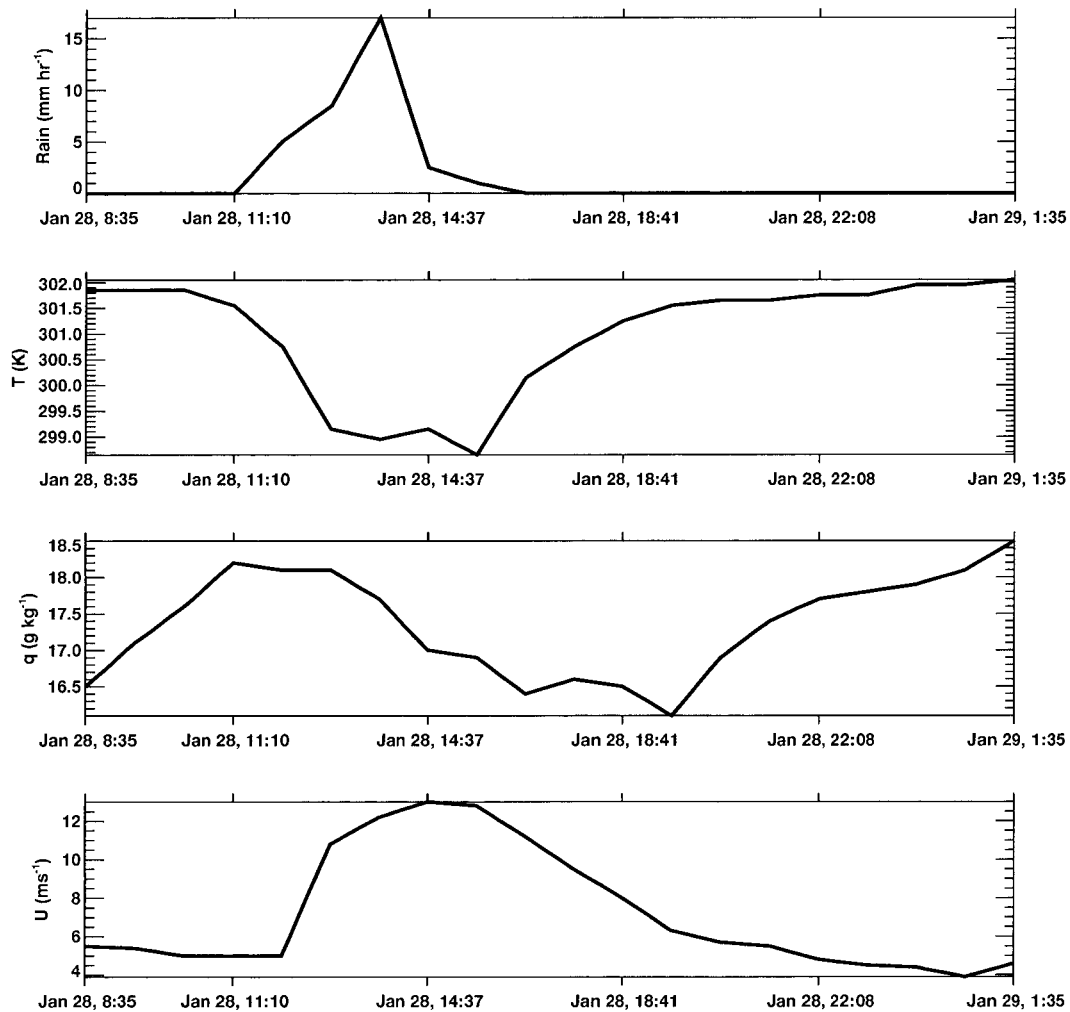


FIG. 17. Rainfall (mm h^{-1}), potential temperature (θ) (K), water vapor mass mixing ratio (g kg^{-1}), and wind speed (m s^{-1}) for a cold pool measured during the TOGA campaign (for details see Young et al. 1995).

attained a horizontal velocity increase of 4.8 m s^{-1} , and the latent and sensible heat fluxes are increased by a factor of 1.9 and 2.6, respectively. The cold pools had a mean lifetime of approximately 2.5 h and attained maximum radii ranging from 3 to 18 km, with a mean of 8.6 km. Taking the organization of convection into account, these figures are consistent with observational studies of convective wakes.

The composite statistics showed that the development of the cold pools consisted of three stages. As observed by Kingsmill and Houze (1999), the boundary layer air in the deep convective inflow region is already higher in θ_e than average. Before the downdraft develops and reaches the subcloud layer, this high- θ_e air can be cooled and moistened by the evaporation of rainfall. This is the reason that the temperature perturbation often occurs before the onset of the moisture perturbation. The downdraft then injects cold and dry air into the boundary layer, and the spreading cold pool is consequentially moister than average just inside the gust front but drier

in the central regions. Finally, mass conservation requires that air from above the boundary layer be entrained into the wake of the expiring downdraft, thus causing the central regions of the cold pool to recover very quickly in temperature, but increases further the moisture perturbation. Many observational studies have confirmed this behavior of cold pools both in terms of the more limited spatial extent of the vapor depression and its delayed onset relative to the temperature perturbation.

The most surprising result of this paper is that in situations of deep convection over the oceans, in low vertical wind shear, the mechanism by which convectively generated cold pools trigger new deep convective cells is completely different from the dynamical lifting role previously assumed. Despite the fact that Rotunno et al. (1988) proposed that cold pool generated circulations without low-level vertical wind shear inhibit deep lifting and would not be conducive for triggering new deep convective cells, this dynamical

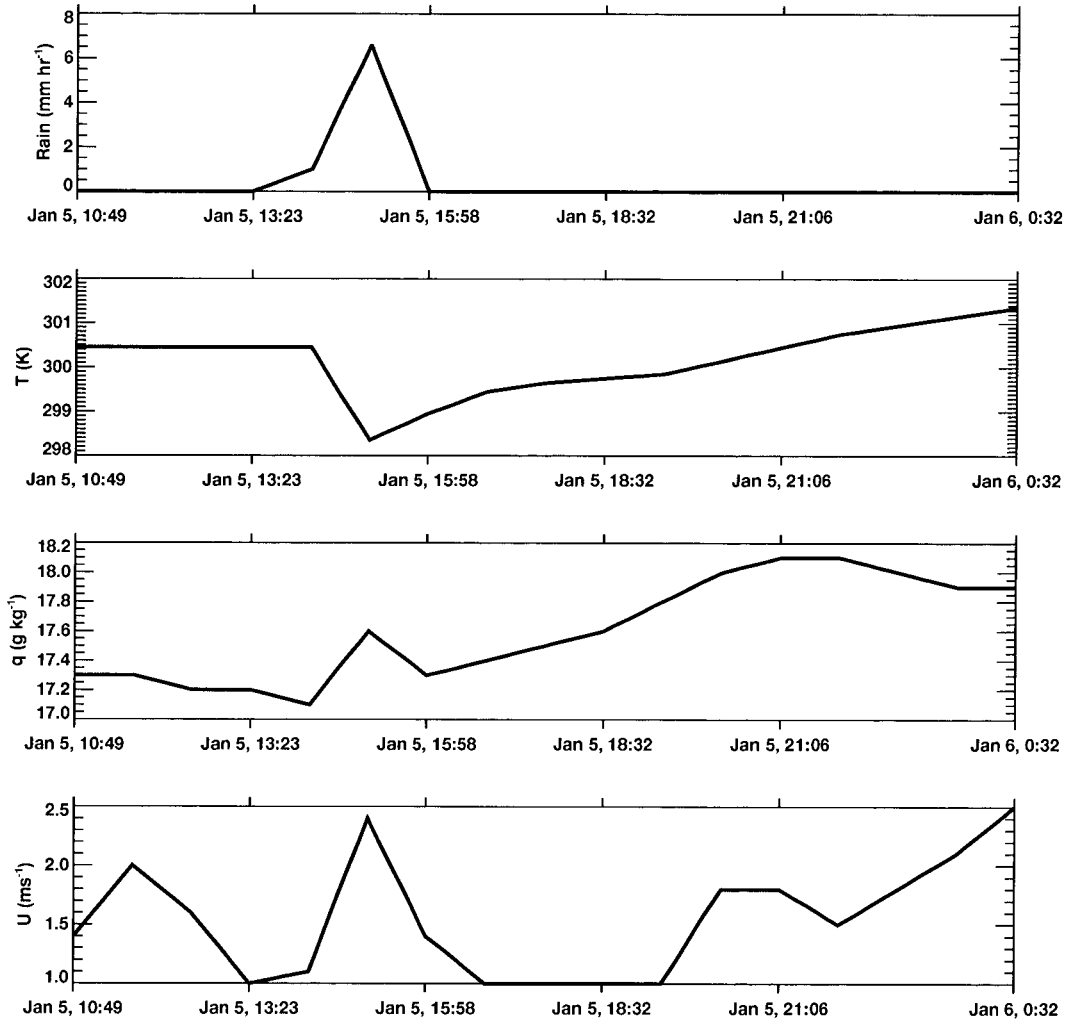


FIG. 18. As Fig. 17 but for a different wake.

role of cold pools has generally been the unique mechanism previously suggested. In fact, the cold pool initiation role in low wind shear situations is very much a thermodynamical one. Cold pools spread to a radius determined by the time taken for surface fluxes to recover the cold pool temperature, thereby reducing CIN. At these radii, the vertical and horizontal velocities are limited, reducing the dynamical uplift of boundary layer air to a minimum. But the cold pool water vapor and θ_e remain higher than in the surrounding environment, despite the turbulent mixing that has occurred during the maturing of the wake. Thus the outer regions of the mature wake are associated with high CAPE values, and low CIN, and therefore any small lifting can easily spawn the next generation of deep convective clouds. Often, the collision of two mature cold pools provides the lifting to initiate new convection. The reason why this role has not been identified from observational data is an obvious one: at the radii at which the cold pools initiate new convection the cold

pool temperature depression is by definition very limited and would be difficult to associate with a specific convective event.

One consequence of the identification of this mechanism is that, since the reduction of cold pool CIN largely determines the radius to which cold pools evolve before they can trigger new events, the organization, or "clustering," of convection is likely to be sensitive to the magnitude of surface fluxes. Further numerical experiments will need to be conducted in order to assess the relative roles of surface fluxes, turbulence mixing, and the evaporation of precipitate in the cold pool evolution.

This paper has highlighted the crucial role that the water vapor field plays in the tropical circulation. Tompkins and Craig (1998) have already shown that the (convectively determined) water vapor field, along with clouds, influences the radiative forcing in such a way as to strongly organize tropical convection. Tompkins (2001) showed how the water vapor field itself directly

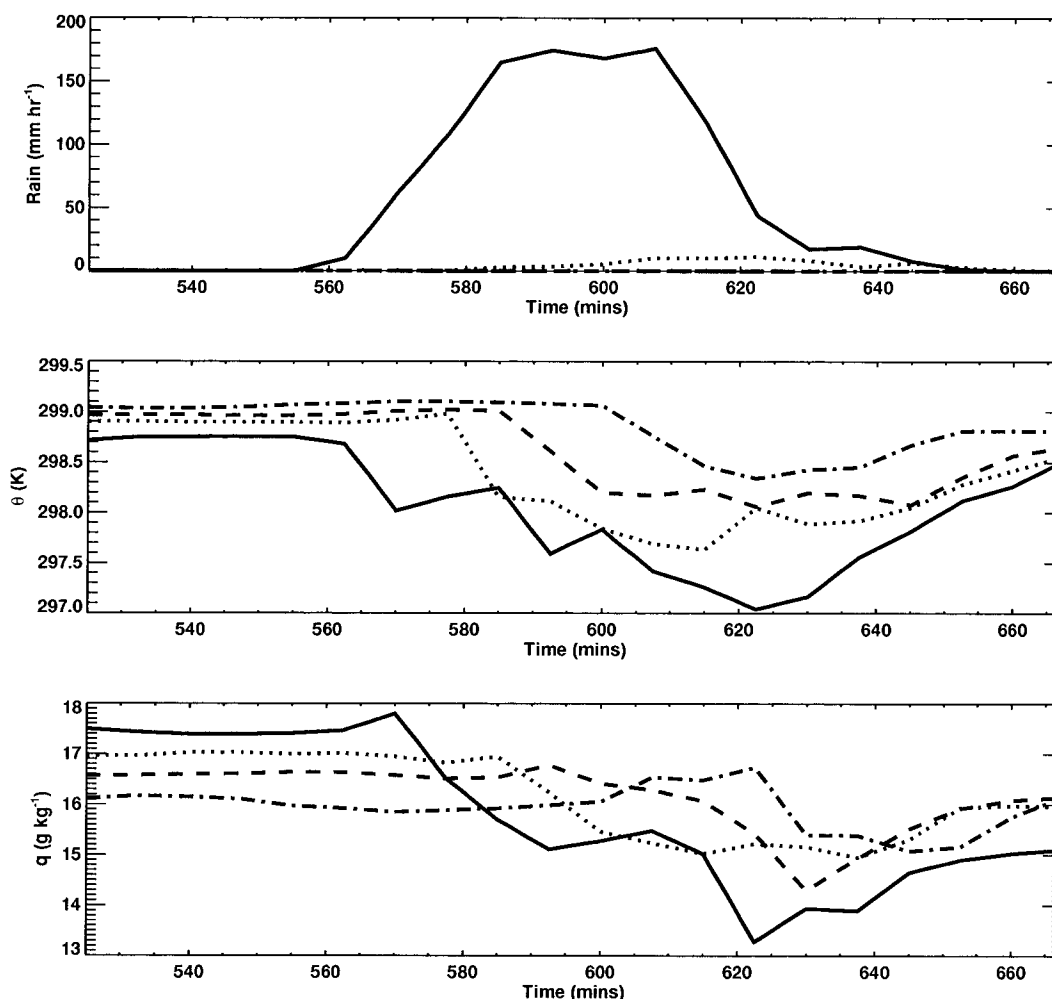


FIG. 19. Time series of rainfall (mm h^{-1}), potential temperature (θ) (K), and water vapor mass mixing ratio (g kg^{-1}) for a cold pool from the CRM experiment. The measurements are taken directly under (solid line), 1.75 km to the west of (dotted), 3.5 km to the north of (dashed), and 5.25 km to the east of (dot-dash) the convective core.

influences the location of convection. This paper has emphasized that even the issue of cold pool dynamics and their initiation of new convective events involves the water vapor field in a central role.

Acknowledgments. Brian Mapes and Wojtek Grabowski provided many comments that helped improve this manuscript, and discussions with Chris Bretherton furthered the author's understanding considerably. George Young is thanked for providing the processed TOGA COARE data; the U.K. Met Office made the cloud-resolving model available; and calculations of CAPE were performed using an adaptation of Kerry Emanuel's code. The author was supported by a European Union Marie Curie Fellowship (FMBICT 983005) and the Max Planck Society during this study.

REFERENCES

- Addis, R. P., M. Garstang, and G. D. Emmitt, 1984: Downdrafts from tropical oceanic cumuli. *Bound.-Layer Meteor.*, **28**, 23–49.

- Barnes, G. M., and M. Garstang, 1982: Subcloud layer energetics of precipitating convection. *Mon. Wea. Rev.*, **110**, 102–117.
- Betts, A. K., 1984: Boundary layer thermodynamics of a High Plains severe storm. *Mon. Wea. Rev.*, **112**, 2199–2211.
- Bony, S., K.-M. Lau, and Y. C. Sud, 1997: Sea surface temperature and large-scale circulation influences on tropical greenhouse effect and cloud radiative forcing. *J. Climate*, **10**, 2055–2076.
- Brown, P. R. A., and H. A. Swann, 1997: Evaluation of key microphysical parameters in three dimensional cloud model simulations using aircraft and multiparameter radar data. *Quart. J. Roy. Meteor. Soc.*, **123**, 2245–2275.
- Brown, R. G., and C. Zhang, 1997: Variability of midtropospheric moisture and its effect on cloud-top height distribution during TOGA COARE. *J. Atmos. Sci.*, **54**, 2760–2774.
- Droegemeier, K. K., and R. B. Wilhelmson, 1987: Numerical simulation of thunderstorm outflow dynamics. Part I: Outflow sensitivity experiments and turbulence dynamics. *J. Atmos. Sci.*, **44**, 1180–1210.
- Emanuel, K. A., 1994: *Atmospheric Convection*. Oxford University Press, 580 pp.
- Fankhauser, J. C., N. A. Crook, J. Tuttle, L. J. Miller, and C. G. Wade, 1995: Initiation of deep convection along boundary layer convergence lines in a semitropical environment. *Mon. Wea. Rev.*, **123**, 291–313.

- Fovell, R. G., and P. H. Tan, 1998: The temporal behavior of numerically simulated multicell-type storms. Part II: The convective cell life cycle and cell regeneration. *Mon. Wea. Rev.*, **126**, 551–577.
- Garratt, J. R., 1992: *The Atmospheric Boundary*. Cambridge University Press, 316 pp.
- Gaynor, J. E., and C. F. Ropelewski, 1979: Analysis of the convectively modified gate boundary layer using *in situ* and acoustic sounder data. *Mon. Wea. Rev.*, **107**, 985–993.
- Geldmeier, M. F., and G. M. Barnes, 1997: The “footprint” under a decaying tropical mesoscale convective system. *Mon. Wea. Rev.*, **125**, 2879–2895.
- Grabowski, W. W., X. Wu, M. W. Moncrieff, and W. D. Hall, 1998: Cloud-resolving modeling of cloud systems during phase III of GATE. Part II: Effects of resolution and the third spatial dimension. *J. Atmos. Sci.*, **55**, 3264–3282.
- Graham, N. E., and T. P. Barnett, 1987: Sea surface temperature, surface wind divergence, and convection over the tropical oceans. *Science*, **238**, 657–659.
- Houze, R. A., and A. K. Betts, 1981: Convection in GATE. *Rev. Geophys. Space Phys.*, **19**, 541–576.
- Jabouille, P., J.-L. Redelsperger, and J. P. Lafore, 1996: Modification of surface fluxes by atmospheric convection in the TOGA COARE region. *Mon. Wea. Rev.*, **124**, 816–837.
- Johnson, R. H., and M. E. Nicholls, 1983: A composite analysis of the boundary layer accompanying a tropical squall line. *Mon. Wea. Rev.*, **111**, 308–319.
- Jorgensen, D. P., and M. A. LeMone, 1989: Vertical velocity characteristics of oceanic convection. *J. Atmos. Sci.*, **46**, 621–640.
- Kingsmill, D. E., 1995: Convection initiation associated with a sea-breeze front, a gust front, and their collision. *Mon. Wea. Rev.*, **123**, 2913–2933.
- , and R. A. Houze, 1999: Thermodynamic characteristics of air flowing into and out of precipitating convection over the west Pacific warm pool. *Quart. J. Roy. Meteor. Soc.*, **125**, 1209–1229.
- Lau, K.-M., H.-T. Wu, and S. Bony, 1997: The role of large-scale atmospheric circulation in the relationship between tropical convection and sea surface temperature. *J. Climate*, **10**, 381–392.
- LeMone, M. A., and E. J. Zipser, 1980: Cumulonimbus vertical velocity events in GATE. Part I: Diameter, intensity and mass flux. *J. Atmos. Sci.*, **37**, 2444–2457.
- , —, and S. B. Trier, 1998: The role of environmental shear and thermodynamic conditions in determining the structure and evolution of mesoscale convective systems during TOGA COARE. *J. Atmos. Sci.*, **55**, 3493–3518.
- Leonard, B. P., 1991: The ULTIMATE conservative difference scheme applied to unsteady one-dimensional advection. *Comput. Methods Appl. Mech. Eng.*, **19**, 17–74.
- Lin, Y. L., R. L. Deal, and M. S. Kulie, 1998: Mechanisms of cell regeneration, development, and propagation within a two-dimensional multicell storm. *J. Atmos. Sci.*, **55**, 1867–1886.
- Liu, C. H., and M. W. Moncrieff, 1996: A numerical study of the effects of ambient flow and shear on density currents. *Mon. Wea. Rev.*, **124**, 2282–2303.
- , and —, 2000: Simulated density currents in idealized stratified environments. *Mon. Wea. Rev.*, **128**, 1420–1437.
- Lucas, C., E. J. Zipser, and M. A. LeMone, 1994: Vertical velocity in oceanic convection off tropical Australia. *J. Atmos. Sci.*, **51**, 3183–3193.
- Mapes, B. E., 1993: Gregarious tropical convection. *J. Atmos. Sci.*, **50**, 2026–2037.
- , 2000: Convective inhibition, subgrid-scale triggering energy, and stratiform instability in a simple tropical wave model. *J. Atmos. Sci.*, **57**, 1515–1535.
- , and R. A. Houze, 1992: An integrated view of the 1987 Australian monsoon and its mesoscale convective systems. Part I: Horizontal structure. *Quart. J. Roy. Meteor. Soc.*, **118**, 927–963.
- , and P. Zuidema, 1996: Radiative–dynamical consequences of dry tongues in the tropical troposphere. *J. Atmos. Sci.*, **53**, 620–638.
- Moncrieff, M. W., 1981: A theory of organized steady convection and its transport-properties. *Quart. J. Roy. Meteor. Soc.*, **107**, 29–50.
- , and E. Klinker, 1997: Organized convective systems in the tropical western Pacific as a process in general circulation models: A TOGA COARE case-study. *Quart. J. Roy. Meteor. Soc.*, **123**, 805–827.
- , and C. H. Liu, 1999: Convection initiation by density currents: Role of convergence, shear, and dynamical organization. *Mon. Wea. Rev.*, **127**, 2455–2464.
- Nair, U. S., R. C. Weger, K. S. Kuo, and R. M. Welch, 1998: Clustering, randomness, and regularity in clouds fields 5. The nature of regular cumulus clouds fields. *J. Geophys. Res.*, **103**, 11 363–11 380.
- Nicholls, S., and M. A. LeMone, 1980: The fair weather boundary layer in GATE: The relationship of subcloud fluxes and structure to the distribution and enhancement of cumulus clouds. *J. Atmos. Sci.*, **37**, 2051–2067.
- Peterson, R. E., Jr., 1984: A triple-Doppler radar analysis of a discretely propagating multicell convective storm. *J. Atmos. Sci.*, **41**, 2973–2990.
- Qian, L., G. S. Young, and W. M. Frank, 1998: A convective wake parameterization for use in general circulation models. *Mon. Wea. Rev.*, **126**, 456–469.
- Randall, D. A., and G. J. Huffman, 1980: A stochastic model of cumulus clumping. *J. Atmos. Sci.*, **37**, 2068–2078.
- Rickenbach, T. M., and S. A. Rutledge, 1998: Convection in TOGA COARE: Horizontal scale, morphology, and rainfall production. *J. Atmos. Sci.*, **55**, 2715–2729.
- Rotunno, R., J. B. Klemp, and M. L. Weisman, 1988: A theory for long-lived squall lines. *J. Atmos. Sci.*, **45**, 463–485.
- Saxen, T. R., and S. A. Rutledge, 1998: Surface fluxes and boundary layer recovery in TOGA COARE: Sensitivity to convective organization. *J. Atmos. Sci.*, **55**, 2763–2781.
- Sengupta, S. K., R. M. Welch, M. S. Navar, T. A. Berendes, and D. W. Chen, 1990: Cumulus cloud field morphology and spatial patterns derived from high spatial resolution Landsat imagery. *J. Appl. Meteor.*, **29**, 1245–1267.
- Simpson, J., 1980: Downdrafts as linkages in dynamic cumulus seeding effects. *J. Appl. Meteor.*, **19**, 477–487.
- Thorpe, A. J., M. J. Miller, and M. W. Moncrieff, 1982: Two-dimensional convection in non-constant shear: A model of mid-latitude squall lines. *Quart. J. Roy. Meteor. Soc.*, **108**, 739–762.
- Tompkins, A. M., 2000: The impact of dimensionality on long-term cloud resolving model simulations. *Mon. Wea. Rev.*, **128**, 1521–1535.
- , 2001: Organization of tropical convection in low vertical wind shears: The role of water vapor. *J. Atmos. Sci.*, **58**, 529–545.
- , and G. C. Craig, 1998: Radiative-convective equilibrium in a three-dimensional cloud ensemble model. *Quart. J. Roy. Meteor. Soc.*, **124**, 2073–2097.
- Weger, R. C., J. Lee, and R. M. Welch, 1993: Clustering, randomness and regularity in cloud fields: 3. Nature and distribution of cloud clusters. *J. Geophys. Res.*, **98**, 18 449–18 436.
- Wilhelmson, R. B., and C.-S. Chen, 1982: A simulation of the development of successive cells along a cold outflow boundary. *J. Atmos. Sci.*, **39**, 1466–1483.
- Xu, Q., M. Xue, and K. K. Droegemeier, 1996: Numerical simulations of density currents in sheared environments within a vertically confined channel. *J. Atmos. Sci.*, **53**, 770–786.
- Xue, M., Q. Xu, and K. K. Droegemeier, 1997: A theoretical and numerical study of density currents in nonconstant shear flows. *J. Atmos. Sci.*, **54**, 1998–2019.
- Yoneyama, K., and T. Fujitani, 1995: The behavior of dry westerly air associated with convection observed during the TOGA-COARE R/V Natsushima cruise. *J. Meteor. Soc. Japan*, **73**, 291–304.

- , and D. B. Parsons, 1999: A proposed mechanism for the intrusion of dry air into the tropical western Pacific region. *J. Atmos. Sci.*, **56**, 1524–1546.
- Young, G. S., S. M. Perugini, and C. W. Fairall, 1995: Convective wakes in the equatorial western Pacific during TOGA. *Mon. Wea. Rev.*, **123**, 110–123.
- Zhu, T., J. Lee, R. C. Weger, and R. M. Welch, 1992: Clustering, randomness and regularity in cloud fields: 2. Cumulus cloud fields. *J. Geophys. Res.*, **97**, 20 537–20 558.
- Zipser, E. J., 1977: Mesoscale and convective-scale downdraughts as distinct components of squall-line circulation. *Mon. Wea. Rev.*, **105**, 1568–1589.